NTNU
Norwegian University of
Science and Technology

Full waveform inversion and wave equation migration using 4D seismic from the Sleipner Field

A CO_2-monitoring study

Amanda Nagypal Bjøringsøy

Petroleum Geoscience and Engineering
Submission date: June 2017
Supervisor: Børge Arntsen, IGP

Norwegian University of Science and Technology
Department of Geoscience and Petroleum

Abstract

In this study, two surveys from the Sleipner field in the North Sea are investigated. The surveys cover the same area, but are acquired at different times - respectively before and after the initiation of CO_2 injection. Since the first injection started in 1996, prominent reflectivity changes as well as large velocity pushdown-effects are observed in the seismic data as a result of the seismic waves traveling slower through the injected gas. The main objectives in this thesis have been to build high-resolution velocity models through acoustic full waveform inversion (FWI) and accurate positioning the subsurface reflectors with one-way wave equation migration (WEM).

The FWI is based on the full wavefield modeling and aims to estimate high-resolution velocity models, by minimizing the difference between observed and modeled data. For this study, the FWI started with a smoothed 1-D velocity model with no lateral changes over the entire dataset. Using refracted energy to update the unknown subsurface velocity, frequency from $2Hz$ up to $12Hz$ were gradually included in the FWI iterations. A background model without the low-velocity gas zone was extracted from the inversion. Colored inversion was used to include the low gas velocities into the model. The two velocity models- with and without the gas zone were then used as input for migration. In contrast to ray-traced migration methods, the WEM is able to handle unsmoothed detailed velocity models for imaging large velocity anomalies. When migrating the monitor data with the colored inversion model, we observed reduced moveout in gathers, thinner layers as well as flatter horizons within the gas plume, compared to migration with the background model. Migration with the colored inversion model also reduced the observed pushdown-effect seen below the gas plume.

A simplified 4D matching of the base and monitor survey was performed prior to the time-lapse study. As the migrated data contained multiples and showed large acquisition footprints, noise and small artifacts in the migrated image may have been magnified as a time-lapse response. This was important to keep in mind when interpreting the time-lapse results. Nevertheless, the CO_2 response itself was very clear, indicating strong confidence in the time-lapse observations. No indication of high amplitude changes in the overburden above the gas was observed, and consequently, no leakage of CO_2 had occurred.

Sammendrag

I dette studiet har to seismiske undersøkelser fra Sleipner feltet i Nordsjøen blitt studert. De seismiske undersøkelsene dekker samme område, men er samlet inn på forskjellige tidspunkt-henholdsvis før og etter starten av CO_2 injeksjon. Siden første injeksjon startet i 1996, har tydelige reflektivitetsendringer og pushdown-effekter blitt observert i dataen av et resultat av at de seismiske bølgene propagerer saktere gjennom den injiserte gassen. Hovedoppgavene i denne masteroppgaven har vært å bygge hastighetsmodeller med høy oppløsning, gjennom akustisk full bølgefelt inversjon (FWI) og nøyaktig plassering av reflektorer med en-vei bølgeligning migrasjon (WEM). FWI er basert på hele bølgefeltet og sikter etter å estimere hastighetsmodeller med høy oppløsning, ved å minimisere forskjellen mellom observert og modellert data. I dette prosjektet startet FWI med en 1-D glattet hastighetsmodell uten endring i horisontal retning over hele datasettet.

Ved å bruke refraktert energi til å oppdatere den ukjente hastigheten, frekvenser fra $2Hz$ opp til $12\ Hz$ ble gradvis inkludert i FWI iterasjonene. En bakgrunnsmodell uten de lave hastighetene ble laget med inversjonen. Farget inversjon ble brukt til å inkludere de lave hastighetene til modellen. De to hastighetsmodellene, med og uten gass, ble deretter brukt som input til migrasjon.

I kontrast til strålebaserte migrasjonsmetoder, klarer WEM å håndtere uglattede detaljerte hastighetsmodeller for å avbilde store hastighetskontraster. Da vi migrerte monitor dataen med den farget inversjonmodellen, observerte vi redusert moveout i gathers, tynnere lag og flatere horisonter inne i gasskyen sammenlignet med migrasjon med bakgrunnsmodellen. Migrasjon med den farget inversjonsmodellen reduserte også pushdown-effekten som var sett nedenfor gasskyen.

En forenklet 4D tilpasning av base og monitor dataen ble utført før time-lapse studiet. Siden dataen inneholdt multipler og viste store innsamlingsfotavtrykk- støy og små feil i det migrerte bilde kan ha blitt forsterket som en time-lapse respons. Dette var viktig å ta i betraktning da vi tolket resultatene. Uansett, CO_2 responsen var veldig klar og tydelig, noe som indikerte gid tiltro til time-lapse observasjonene. Ingen indikasjon på høye amplitudeforandringer i det grunne ble observert og derfor har ikke lekkasje av CO_2 funnet sted.

Preface

This paper has its origin in the Master thesis that students in their last year at the Norwegian University of Science and Technology have to submit as part of their study program. The paper was written during spring 2017 with a time frame of 20 weeks. The report was written in cooperation with PGS.

Trondheim, 2017-06-11

Amanda N. Bjøringsøy

Acknowledgment

I would like to thank PGS for permission to present this work. I am deeply grateful for the extraordinary close and careful guidance from Julien Oukili, Grunde Rønholt and Øystein Korsmo. Without their involvement, support and valuable discussions, this thesis would not have been possible. Special thanks to Julien, who has been my adviser at PGS and supported me throughout the work with this thesis. I would also like to thank Stine Indrebø and the rest of the Imaging team for the warm welcome to PGS and taking good care of me.

The Sleipner license; Statoil ASA, ExxonMobil Exploration and Production Norway AS, LOTOS Exploration and Production Norge AS and KUFPEC Norway AS are acknowledged for allowing me to use the Sleipner data.

I would like to thank Marianne Houbiers, Roya Dehghan Niri and Anne-Kari Furre from Statoil Rotvoll for their involvement during the study and their comments and suggestions for further improvement. Their help and guidance have been much appreciated.

I would also like to thank my PGS colleagues Ilyes Bouzid, Berit Mattson and Åse Sollid for valuable help during my work in PGS, and for making helpful suggestions when problem arose, and providing me necessary data or material when needed.

Iina Kristensen, Tony Nagypal and Arnstein Kvilhaug are being thanked for reading correction.

Finally, I give my thanks to Professor Børge Arntsen, who has been my supervisor during the master thesis. Thank you for great supervision during the process of writing my thesis.

Contents

Chapter 1

Introduction

Accurate velocity estimation is thought by many to be the major challenge when imaging the subsurface geology for petroleum exploration. Both time and depth migration need an estimate of the subsurface velocity, in order for the migration process to succeed. An incorrect velocity model may not produce an interpretable image. Unwanted structures or artifacts, change in dips or moving horizons to incorrect depths are problems relating to incorrect velocities. For more demanding migration techniques the need for an accurate velocity model is even more important. In this study, we present a CO_2-monitoring study with acoustic full waveform inversion to gain high resolution velocity models and wave equation migration for accurate imaging the subsurface reflectors.

This paper will start with objectives and limitations in chapter 2. Then background of the Sleipner field and the inversion area together with a description of the seismic datasets are presented in chapter 3. In the next chapter, chapter 4, the theories for the different seismic applications which have been used in the study are explained. Finally, the results are presented in chapter 5. In the first section, section 5.1, precondition of the seismic data is presented. In the following section, section 4.2, the full waveform inversion is introduced. When high-resolution velocity models from the inversion are extracted, one-way wave equation migration is applied as seen in section 4.3. After the migration, simplified time-lapse study is performed as showed in section 5.4. We conclude the report with a discussion and a final conclusion in chapter 6 and 7.

Chapter 2

Background

2.1 Objectives

The main objective of this Master study is to build high-resolution velocity models through full waveform inversion by pushing the frequency to an upper limit. As the seismic waves travel slower through the injected gas, velocity pushdown-effects are visible in the seismic. The velocity model built from full waveform inversion should be able to include the low-velocity zone caused by the injected gas, and remove the large pushdown-effect observed in the seismic. A background model, without the low velocity zone should also be extracted from the inversion and used for migrating the base survey.

With the two different models, the background model and the model including the gas, one-way wave equation migration should be performed on both surveys.

After the migration, the third objective is to calculate time-lapse differences between the two surveys and detect potential gas leakage to the overburden.

2.2 Limitations

As computer power costs have become less of an issue over the last decade, full waveform inversion and one-way wave equation migration have become more common to use especially for small surveys. Full waveform inversion is relatively simple to write, but in practice if the data is big and many iterations are needed for construction of the velocity model, the extra computational cost may be dramatic.

The data used in this project was very small compared to commercial projects, giving an opportunity to use full waveform inversion and wave equation migration. Still, the time frame of 20 weeks was the biggest limitation for the study. More time could have been used at every processing step, and especially when creating the initial velocity model used for full waveform inversion.

The final demultiple data was not available by the time of the project initiation. Instead, partially finished demultiple data for both datasets was provided and used for migration. This means that the migration was performed using data with remaining multiples and hence unwanted noise or artifacts may have been introduced to the migrated image. This must be taken into account, especially when interpreting the time-lapse results, as such artifacts can be magnified and create false time-lapse results.

Limitations within the codes itself are usually due to avoidance of increasing componential cost. The full waveform inversion used in this study, was based on the acoustic wave equation and so it neglects share waves. Also, the migration algorithm used is based on a one-way approximation of the full two-way wave equation. These approximations and limitations of the different algorithms are further analyzed in the discussion, chapter 6.

Chapter 3

The Sleipner Data

3.1 Background

The Sleipner field is located in the Norwegian sector of the North Sea in block 15/9. After its discovery in 1974 several platforms have been installed and Sleipner is today considered as one of Norway's largest gas fields. The field consists mainly of the two large fields; Sleipner Vest gas field and Sleipner Øst gas condensate field, together with several smaller fields nearby. Figure 3.1 shows the location of the Sleipner field and the study area. The gas produced from Sleipner Vest contains around 4-9.5% of CO_2 (Baklid et al., 1996) and is transferred to Sleipner Øst where the CO_2 is stripped off the gas and injected to the Utsira Formation at around $1000m$ depth, above the producing reservoir. More than 12 millions tons of carbon dioxide have been stored in the Utsira Formation since

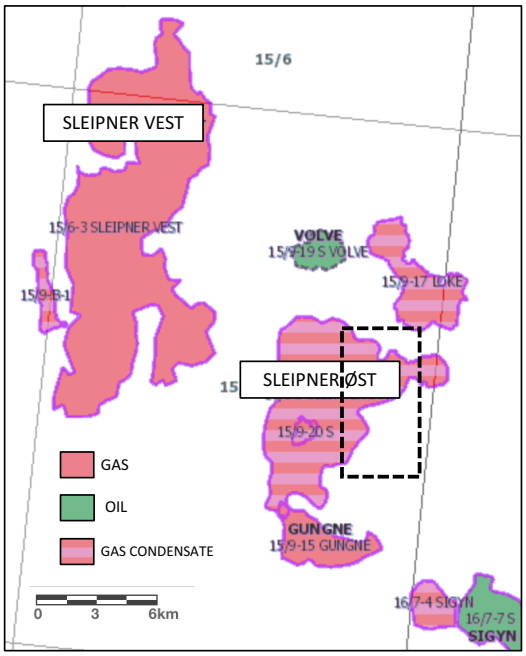

Figure 3.1: Map of the Sleipner fields. The study area is located near Sleipner Øst and is marked with a black dashed rectangle. Map courtesy of the Norwegian Petroleum Directorate

the initiation of CO_2 injection in 1996 (Furre and Eiken, 2014). A seismic survey from 1994 covers the Sleipner area before the injection of carbon dioxide started and is used as a baseline. After this, eight surveys have been acquired to monitor the CO_2 behavior in the Utsira Formation. The formation consists of a porous and permeable sandstone with a thickness of about 200-300 meters. It has previously been interpreted that the CO_2 is stored in several thin super-imposed layers of sand and shale (Furre and Eiken, 2014). The CO_2 saturation introduces a significant change in acoustic impedance, which is easily visible in the monitor data. Nevertheless, it has been previously difficult to get accurate and reliable images of the CO_2 and underlying sediments due to the unknown gas velocity.

3.2 Acquisition

The two seismic surveys used in this project were acquired in 1994 and 2010. The oldest survey from 1994 was acquired using conventional streamers, while the seismic survey from 2010 was acquired with PGS's towed dual sensor streamer, GeoStreamer, and is used as a monitor survey. As the full waveform inversion was only performed using the monitor survey, important acquisition parameters for this dataset will be described. For base survey acquisition parameters, the reader is referred to table 3.2. The recorded trace length for the monitor survey is $4608ms$ and is sampled every $2ms$. Note that all figures in the report will be cut at maximum $2000ms$ or $2000m$ even though more recorded data was used in the processing. The dataset was acquired using 12 streamers with a separation of $75m$ and each streamer had respectively 480 receivers. In the provided data used in this study, the streamer length was cut so only 456 receivers per streamer were included. The sources were towed at $5m$ and fired every $12.5m$. The raw hydrophone data consisted of 6200 shots which were spread over 10 sequences.

Survey	ST94	ST10
Shooting direction	0.853°	0.853°
Source depth	6	5
No. of sources	2	2
Shot interval	18.75 m	12.5 m
Streamer depth	8 m	15 m
No. of streamers	5	12
Streamer separation	100	75 m
No. of receivers per streamer	240 Only 230 available for this study	480 Only 456 available for this study
Receiver separation	12.5 m	12.5 m
Min offset	237 m	85 m
Recorded trace length	5500 ms	4608 ms

Figure 3.2: Acquisition parameters for the base (ST94) and monitor survey (ST10). Note that the surveys were acquired with different acquisition geometry.

3.3 Inversion area

The two surveys covered approximately the same area, which was $9km\ x\ 4km$. The raw hydrophone data from the monitor survey was spread over 10 sequences as showed in figure 3.3. In what follows, all inline and xline ranges are given with respect to the ranges in this figure. The shot interval was $12.5m$ and the shooting direction was 0.853^o as can be seen on the slightly rotated grid in the figure. The odd shape of the acquisition was caused by the five sequences in the middle, which were acquired in the opposite direction from the other sequences. The study area consists of relatively flat sediment layers, but in the shallow part, paleo fluvial systems are visible. A shallow subsurface image at depth of $240m$ is

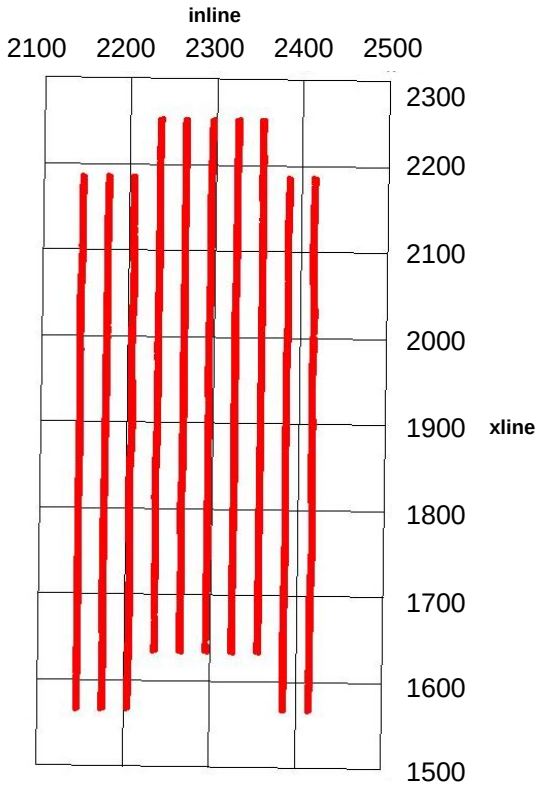

Figure 3.3: Acquisition outline for the monitor survey.

shown in figure 3.4 (see figure B.1 in appendix for inline and xline location). Several channels in different sizes are visible trending northwest-southeast. The gas cloud becomes visible at around $800m$ and is most prominent at $900m$ as seen in figure 3.5. Figure 3.6 shows one shot recorded at the middle cable coming from the CO_2 plume with different frequency bands. The full bandwidth is displayed in figure 3.6 a). The near offset shows several clear reflections before they get masked by the high amplitude refracted arrivals. It is most likely that the near offset is dominated by reflected multiples. The first frequency band used for full waveform inversion was 2-6Hz as illustrated in figure 3.6 b). Here the linear events, such as direct arrival, refraction or diving waves, are smeared out and it is hard to distinguish them. At this frequency band, the shallow reflections are more or less not visible. As the frequency band increases (figure 3.6 c and d) more events become visible. Still, the near offset reflections are not very obvious even at 2-12Hz.

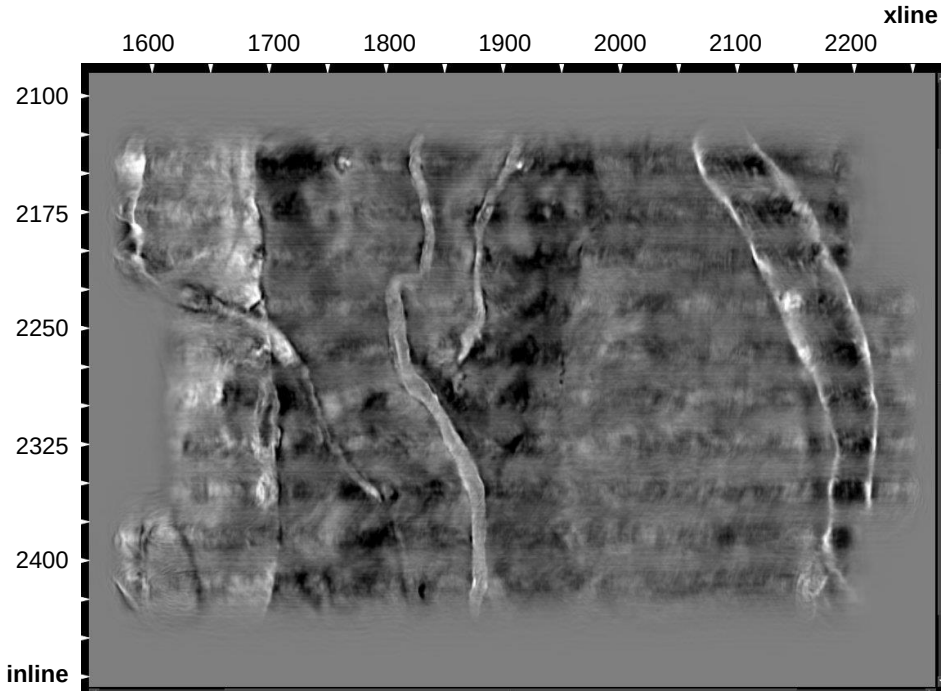

Figure 3.4: Depth slice at 240m showing widespread presence of channels of varying scales.

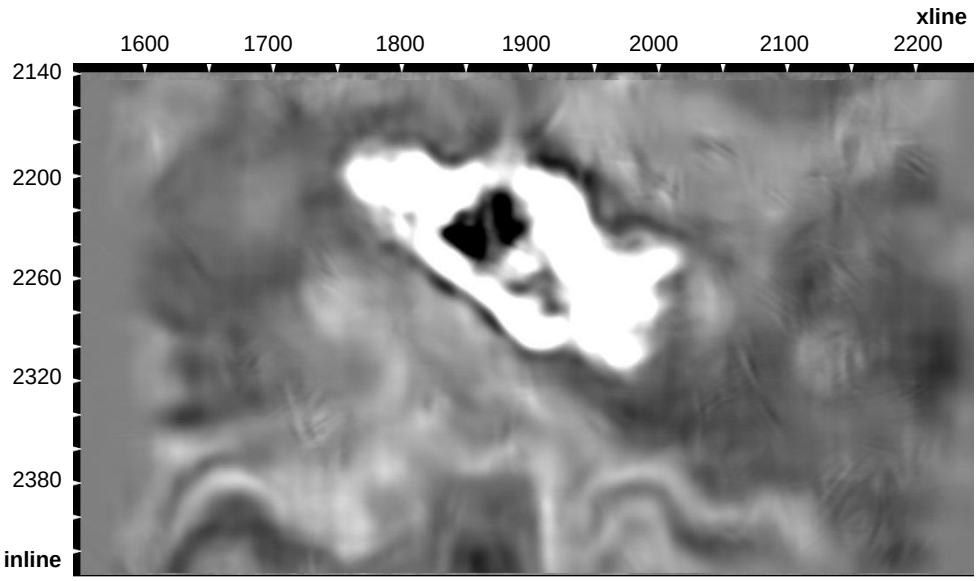

Figure 3.5: The gas cloud is easily seen at depth 900m.

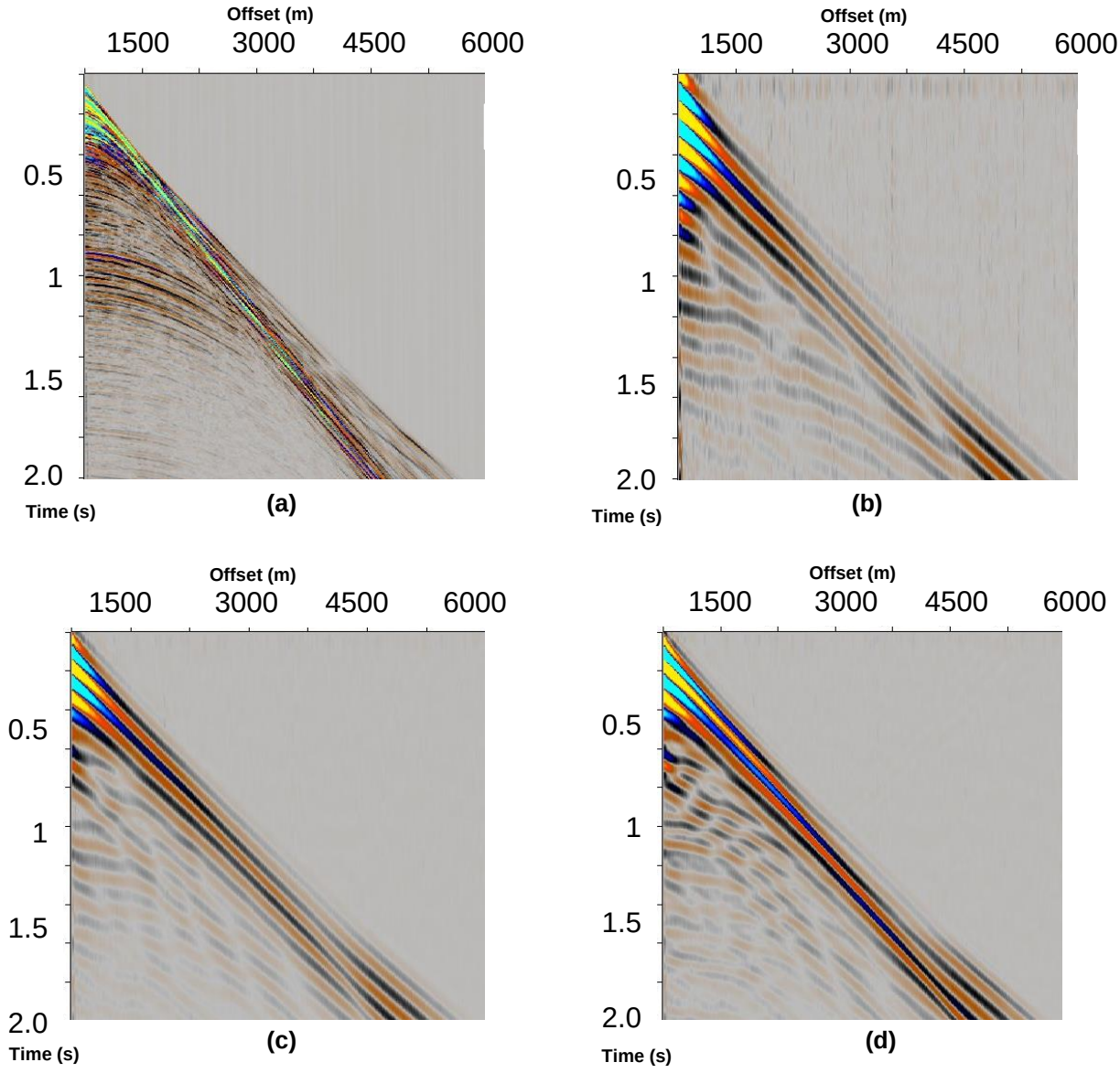

Figure 3.6: Shot gathers from the gas plume with different frequency bands. **(a)** Full bandwith, **(b)** 2-6Hz, **(c)** 2-9Hz, **(d)** 2-12Hz.

Chapter 4

Theory

4.1 Denoise

Recorded data from a seismic vessel will always contain both signal and noise. The noise may be coherent such as multiples, incoherent such as swell noise or random such as streamer noise. The presence of noise in the data may mask and distort the desired signals and cause difficulties for the processor. It is therefore important to attenuate the noise for improving the signal to noise ratio (S/N) and gain best possible resolution for a more accurate image. In this study, as the full waveform inversion will generate multiples in the forward modeling using the free surface, the raw hydrophone data was used. The forward modeling would on the other hand *not* model other noise, so these signals needed to be removed prior to inversion. In the data used for this project the shots were mainly contaminated by swell noise and some linear noise.

Swell noise comes from a formation of long wavelength surface waves on the sea. They are typically more stable in both direction and frequency than normal oceanic waves because they are created by tropical storms and stable wind systems. The main characteristics with swell noise are the low frequency component, often between 0-5Hz and high amplitude "stripes" seen in shot gathers. PGS has implemented a swell noise attenuation method, which is designed to attenuate all types of incoherent noise that are characterized by large amplitudes in the frequency spectrum, compared to the signal that we want to preserve. By first detecting the noisy ampli-

tudes for then to replace these by interpolated values using FX predictive filtering, the incoherent noise gets attenuated.

Typical characteristics with linear noise are low amplitude, coherent, linear dipping, low frequency and they are often stronger at the far offsets. Linear noise can be attenuated with for example FK-polygon to model the noise and then subtract from the data. By defining a polygon in the FK domain using wavenumber and frequency pairs around the noisy zone, the noise within the polygon can be subtracted from the data.

4.2 Beam migration

In this study, Beam migration has worked as a quality tool. The migration algorithm produces images and gathers fast and accurately. The Beam migration is based on ray-theory and uses ray tracing as a shortcut to "play the waves back into the ground". It assumes that all energy travels between two points along a line, a ray, which follows the shortest travel time path between two points. The migration is an integral approximate solution of the wave equation where source impulse is assumed.

4.3 Full waveform inversion

Full waveform inversion (FWI) deals with arrival times, as in tomography, but also uses the information around phase and amplitude for both reflected and refracted waves measured in the seismic data. The velocity analysis procedure is based on the full wavefield modeling and aims to estimate high-resolution velocity models, by minimizing the difference between observed and modeled seismic data. In most cases, the use of the full wavefield will provide a more detailed velocity model than conventional reflection tomography, or PSTM, and gain more resolution especially in the shallow part where reflection-based velocity estimation methods tend to suffer.

Conventional FWI relies mostly on refracted energy and diving waves and not reflected data.

The algorithm used in this study is PGS's new robust method for recovering long-wavelength updates in gradient-based FWI (Ramos-Martinez et al., 2016). The method can use both transmitted as well as reflected energy in a global FWI scheme to provide high-resolution velocity models without migration imprint in the updates. The gradient is computed by applying dynamic weights in the velocity sensitivity kernel which is derived from impedance and velocity parameterization of the objective function. The new approach needs the low wavenumber components to provide velocity updates beyond penetration depth of diving waves so the use of a velocity kernel is ideal for FWI since the velocity kernel is able to separate the low from the high wavenumber components.

4.3.1 Forward problem

The modeled seismic data is reached in the forward modelling by solving the acoustic wave equation with a selected starting model $\mathbf{m_0}$.

$$\nabla^2 \mathbf{P_S}(\mathbf{x}, t) - \frac{1}{\mathbf{m_0}^2(\mathbf{x})} \frac{\partial^2 \mathbf{P}_S(\mathbf{x}, t)}{\partial t^2} = S(\delta(\mathbf{x} - \mathbf{x_S}) f(t - t_0)) \tag{4.1}$$

where $\mathbf{P_S}$ is the source wavefield, $\mathbf{x}$ is spatial coordinates, t is time, $\mathbf{x_S}$ represents the source location, t_0 is the start time and S is the source.

The solution of the wave equation is found by numerical finite difference method. Solving the wave equation with finite difference is considered as the classical and most frequently used method for the numerical simulation of the wave equation.

4.3.2 FWI as a least-squares local optimization approach

The difference between the observed and forward modeled data can be described by a misfit function. The goal in FWI is to find the minimum of the misfit function and then reproduce the same events at the same locations as seen in the real data (Virieux and Operto, 2009), (Fichtner, 2010), (Ramos-Martinez et al., 2016). The theory behind the method is based on the assumption

that the modeled data can be generated from a velocity model **m** using the wave equation.

A linear geophysical modelling process may be described as a linear system:

$$\mathbf{Am} = \mathbf{d} \tag{4.2}$$

where **A** describes the modelling operator which maps **m** to **d**. **d** corresponds to the observed data, while **m** is a matrix containing some physical parameters related to the observed data that can be thought of as the velocity model or the subsurface reflectivity.

The aim of geophysical inversion is to find the unknown matrix that contains the right parameters of the subsurface. This can be illustrated by using the inverse of the modelling operator.

$$\mathbf{m} = \mathbf{A}^{-1}\mathbf{d} \tag{4.3}$$

However, in practice, it is not possible to find an explicit expression for the inverse operator. The FWI solution to solve the inverse problem in equation 4.3 is to consider it as an optimization approach where the difference between observed and modeled data is described by a misfit function, see equation 4.4.

The misfit function is non-linear and the minimum of the function is sought in the vicinity of the starting model $\mathbf{m}_0$. With a normalized version of the standard least-squares norm as the objective function, the function is defined as (Raknes, 2015a)

$$\varphi(\mathbf{m}) = \frac{1}{2}\sum_s \sum_r ||\mathbf{A}(\mathbf{m_0})_{s,r} - \mathbf{d}_{s,r}||^2_{min} \tag{4.4}$$

Where $\varphi(\mathbf{m})$ defines the misfit function and $\mathbf{s},\mathbf{r}$ represents the source and receiver location. The misfit function $\varphi(\mathbf{m})$ is nonlinear, but can be expressed by a second order Taylor development in the vicinity of the starting model $\mathbf{m_0}$ to gain a linear structure.

$$\varphi(\mathbf{m}) \approx \varphi(\mathbf{m_0}) + \frac{\partial\varphi(\mathbf{m_0})}{\partial\mathbf{m}}(\mathbf{m}-\mathbf{m_0}) + \frac{1}{2!}\frac{\partial^2\varphi(\mathbf{m_0})}{\partial\mathbf{m}}(\mathbf{m}-\mathbf{m_0})^2 + \mathcal{O}(\mathbf{m^3}). \tag{4.5}$$

By keeping the first derivative in equation 4.5 and then derive the expression with respect to the model parameter results in

$$\frac{\partial\varphi(\mathbf{m})}{\partial\mathbf{m}} = \frac{\partial\varphi(\mathbf{m_0})}{\partial\mathbf{m}} + \frac{\partial^2\varphi(\mathbf{m_0})}{\partial\mathbf{m^2}}(\mathbf{m}-\mathbf{m_0}). \tag{4.6}$$

The difference between the real model and starting model is described by $\Delta\mathbf{m}$: $\Delta\mathbf{m} = \mathbf{m}-\mathbf{m_0}$. The minimum of the misfit function is reached when the derivative of the misfit function is equal to zero.

$$0 = \frac{\partial\varphi(\mathbf{m_0})}{\partial\mathbf{m}} + \frac{\partial^2\varphi(\mathbf{m_0})}{\partial\mathbf{m^2}}\Delta\mathbf{m} \tag{4.7}$$

Rearranging and taking the inverse of the second order derivative of the misfit function gives:

$$\Delta\mathbf{m} = -\left(\frac{\partial^2\varphi(\mathbf{m_0})}{\partial\mathbf{m^2}}\right)^{-1}\frac{\partial\varphi(\mathbf{m_0})}{\partial\mathbf{m}}. \tag{4.8}$$

The Hessian matrix, $\mathbf{H}$, is defined as the second order derivative of the misfit function with respect to the model parameter $\mathbf{m}$ so that equation 4.8 becomes:

$$\Delta\mathbf{m} = -\mathbf{H}^{-1}\frac{\partial\varphi(\mathbf{m}_0)}{\partial\mathbf{m}} \tag{4.9}$$

In equation 4.10, $\mathbf{g}$ is described as the gradient of the misfit function with respect to the starting model.

$$\Delta\mathbf{m} = -\mathbf{H}^{-1}\mathbf{g} \tag{4.10}$$

Inverting a large matrix is computer demanding and solving the problem by computing the Hessian directly is not possible. The Hessian matrix is therefore often approximated as a diagonal matrix multiplied with a step length α.

$$\mathbf{H}^{-1} \approx \alpha\mathbf{I} \tag{4.11}$$

For conventional FWI, the model obtained after the first iteration of the local optimization looks like a migrated image obtained by reverse time migration (Virieux and Operto, 2009).

PGS's have implemented a gradient approach where the model parameters are adjusted in small steps leading to the minimum of the misfit function with a steepest decent solution (Ramos-Martinez et al., 2016).

Since the relationship between the data and the model is nonlinear, the approach needs to be iterated several times to reach a minimum of the misfit function. The update of the model for each inversion is given by

$$\mathbf{m}_{k+1} = \mathbf{m}_k - \mathbf{H}_k^{-1}\mathbf{g}_k \tag{4.12}$$

where $\mathbf{m}_{k+1}$ is the updated model and $\mathbf{H}_k^{-1}$, $\mathbf{g}_k$ and $\mathbf{m}_k$ is the Hessian matrix, the gradient and the model at step k.

Convectional FWI calculates the gradient by cross-correlation of the forward propagated source wavefield and the back propagated receiver wavefield, see 4.13:

$$g(\mathbf{x}) = \frac{1}{A(\mathbf{x})}\int_t \mathbf{P_S}(\mathbf{x},t)\mathbf{P_R}(\mathbf{x},T-t)\,dt \tag{4.13}$$

where g is the gradient, A represents normalization for source illumination, $\mathbf{P_S}$ is the source wavefield, $\mathbf{P_R}$ is the receiver wavefield, x is the spatial coordinated which can be described by $\mathbf{x} = (x, y, z)$ and t represents time. PGS new gradient based FWI effectively eliminates the migration isochrones produced by the specular reflections and enhances the low wavenumber components in the gradient in heterogeneous media. Now the gradient is calculated by dynamically weighting the velocity kernel. The velocity kernel is defined by, see equation 4.14

$$K_v(\mathbf{x}) = K_K(\mathbf{x}) - K_\rho(\mathbf{x}) \tag{4.14}$$

were K_K is the bulk modulus kernel and K_ρ is the density kernel. The kernels are defined by:

$$K_K(\mathbf{x}) = \frac{1}{\kappa(\mathbf{x})} \int \frac{\partial \mathbf{P_S}(\mathbf{x}, t)}{\partial t} \frac{\partial \mathbf{P_R}(\mathbf{x}, T-t)}{\partial t} dt \tag{4.15}$$

and

$$K_\rho(\mathbf{x}) = \frac{1}{\rho(\mathbf{x})} \int \nabla \mathbf{P_S}(\mathbf{x}, t) \cdot \nabla \mathbf{P_R}(\mathbf{x}, T-t) dt. \tag{4.16}$$

Then, equation 4.14 can be written as (Ramos-Martinez et al., 2016):

$$g(\mathbf{x}) = \frac{1}{2A(\mathbf{x})} \int \Big[- W_1(\mathbf{x}, t) \nabla \mathbf{P_S}(\mathbf{x}, t) \cdot \nabla \mathbf{P_R}(\mathbf{x}, T-t) + W_2(\mathbf{x}, t) \frac{1}{\mathbf{m}^2(\mathbf{x})} \frac{\partial \mathbf{P_S}(\mathbf{x}, t)}{\partial t} \frac{\partial \mathbf{P_R}(\mathbf{x}, T-t)}{\partial t} \Big] dt \tag{4.17}$$

where $W_1(\mathbf{x}, t)$ $W_2(\mathbf{x}, t)$ are the dynamic weights designed to optimally suppress the migration isochrones. In reality, there exist more than one minimum and it may cause the FWI to converge to a local minimum. The gradient approach requires that the starting model for FWI is within the basin or flanks of the minimum of the misfit function, see figure 4.1. This problem can be avoided with a precise and accurate staring model that places the model close to the global minimum. Also, the very low frequency part of the seismic data should be used in the inversion first because it will increase the area around the global minimum and "filter out" some of the other local minimums (Ramos-Martinez et al., 2016). The frequency content for inversion should be increased, only when the misfit function is desirable low, and hence the modeled data match well with the real data.

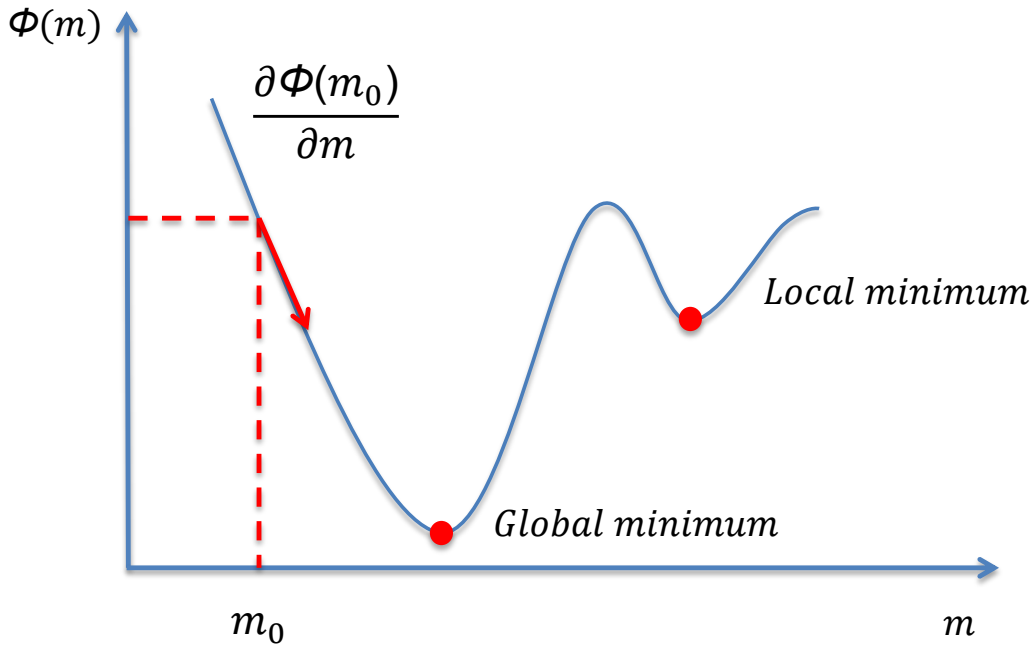

Figure 4.1: It is important that the initial model is within the flanks of the global minimum of the misfit function, otherwise it can be trapped within a local minimum.

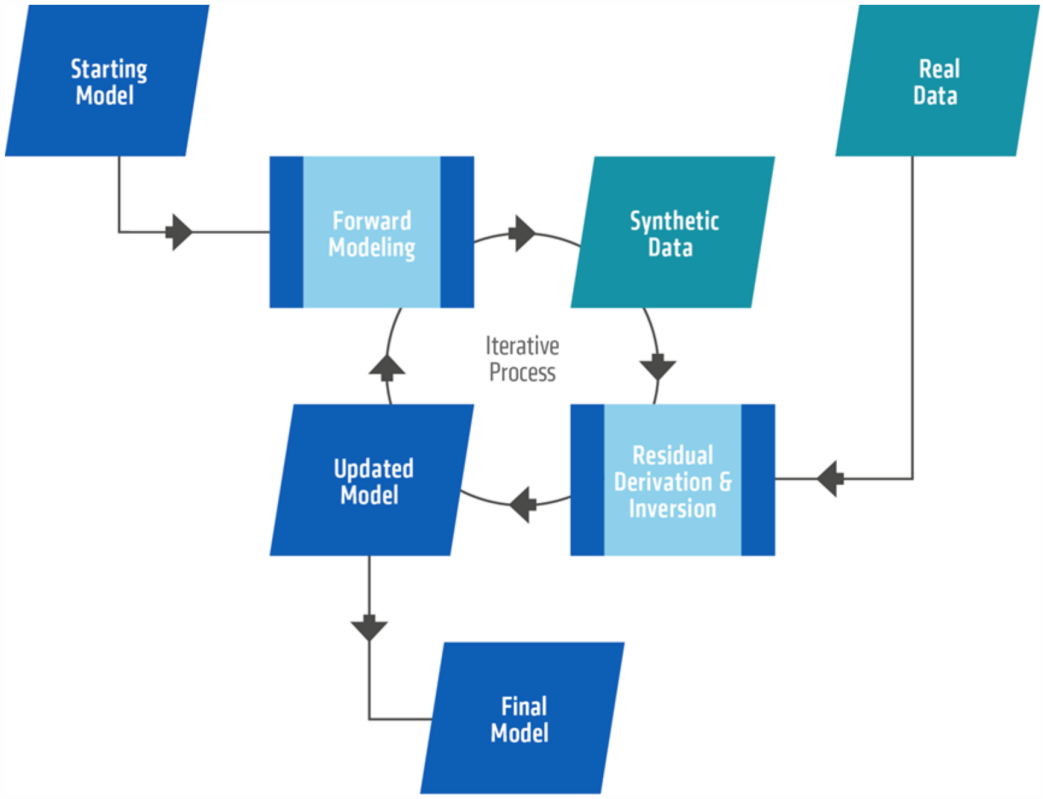

Figure 4.2: Full waveform inversion workflow. First, modeled shots are computed with the initial starting model. Then a comparison of the modeled and observed data is used to generate an objective function based on the residual scalar error. After inversion, the updated model is then used as the new starting model. The iterative process stops when the difference between modeled and real data is desired low and hence the model has converged to a solution. *(Illustration from PGS, 2017)*

4.4 One-way wave equation migration

Wave equation methods naturally consider the whole wavefield from the surface to the image point as seen in contrast to ray-traced migrations where the migrations only calculate one straight ray-paths from the source and receiver to the image point. In this study, one-way wave equation migration (WEM) have been applied. WEM solves the one-way wave equation in the frequency domain, one depth slice at a time. A simple understanding of the one-way propagation methods will only deal with energy that is upcoming. This will exclude many arrival paths, such as multiples, diving waves and refractions since these waves have undergone dou-

ble bounces or continuous refraction (Jones, 2010).

The WEM algorithm requires a wavefield extrapolator, which solves the one-way approximation of the full (two-way) wave equation in the frequency domain, one depth slice at a time as seen in figure 4.3.

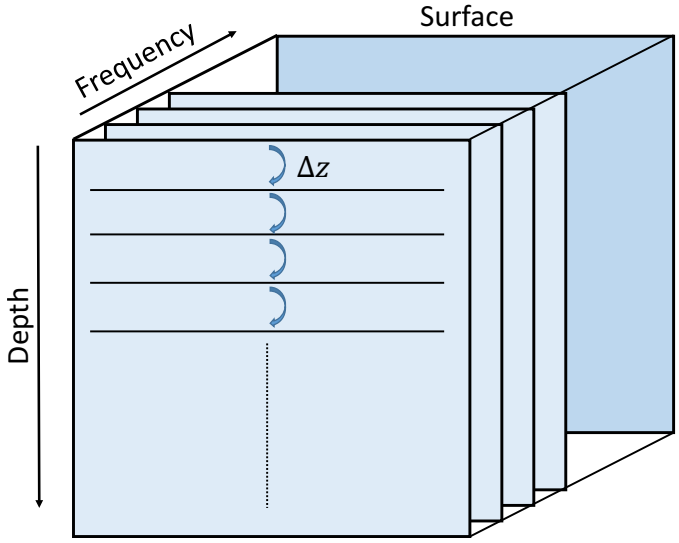

Figure 4.3: WEM uses only several 2D arrays (frequency slices) to extrapolate the wavefields in the frequency domain, one depth slice at a time.

For a 2D acoustic Earth model, the full wave equation in the (ω, x, z) domain is of the following form:

$$\frac{\partial^2 P}{\partial x^2} + \frac{\partial^2 P}{\partial z^2} = -\frac{\omega^2}{c^2} P \tag{4.18}$$

where P is the wavefield, x is horizontal coordinate, z is depth, c is velocity and ω the angular frequency.

The first step for WEM is to downward-propagate the source wavefield and the recorded wavefield from the surface into the subsurface by solving the one-way wave equation using plane waves in the frequency domain. Plane waves are represented by (Arntsen, 2015)

$$exp(i\omega t - ik_x x \pm ik_z z) \tag{4.19}$$

where ω is the angular frequency, k_x and k_z is the horizontal and vertical wavenumber.

The vertical wavenumber can be expressed by the horizontal wavenumber, the angular frequency, and the velocity

$$k_z = \sqrt{\omega^2/c^2 - k_x^2} \tag{4.20}$$

After a 2D Fourier transform with respect to time and lateral distance the two-way wave equation 4.18 can be divided into upgoing and downgoing wavefields.

The downgoing wavefield P_S:

$$P_S(z) = e^{ik_z z} \tag{4.21}$$

and the upgoing wavefield P_R:

$$P_R(z) = e^{-ik_z z} \tag{4.22}$$

WEM expresses the wavefield at a particular depth in terms of the same wavefield existing at a shallower or greater depth to the recorded wavefield and the wavefield coming from the source location. Then for the next depth step after the surface, the downgoing wavefield can be expressed by the wavefield at the source location, $z = 0$

$$P_S(k_x, z + \Delta z, \omega) = P_S(k_x, z, \omega) e^{ik_z \Delta z} \tag{4.23}$$

and the upcoming wavefield

$$P_R(k_x, z + \Delta z, \omega) = P_R(k_x, z, \omega) e^{-ik_z \Delta z}. \tag{4.24}$$

Equation 4.23 and 4.24 summarizes the familiar phase shift method (Gazdag, 1978). With the

upcoming and downgoing wavefield, the algorithm uses cross-correlation imaging condition[1] to accurate image the subsurface reflectively.

4.5 Time-lapse seismic to monitor CO_2 injection

4D seismic, or often called time-lapse seismic, is repeated seismic surveys over a producing hydrocarbon field to monitor production related changes. Time-lapse seismic is also used for monitoring injection of carbon dioxide to subsurface reservoirs. The increased environmental focus on greenhouse emissions has made the understanding of the gas behavior extremely important. Several successful storage projects have shown that huge amounts of CO_2 can be injected to subsurface saline aquifers and stored. But the injection process is both time-consuming, data demanding and cost-expensive. The fear of leakage to the overburden and other damages to the nearby environment are regarded as important issues that must be avoided. It is therefore easy to understand the commercial value of such a tool as time-lapse data. The repeated surveys give an understanding of the subsurface changes and valuable information to future injection planning. The first acquired survey is usually called the baseline survey and the repeated survey is called monitor survey. Ideally, the base survey is acquired before production or injection from the stated field, while the monitor survey is acquired after some time. The time-lapse difference is calculated by subtracting the monitor survey from the base survey or vice versa. The difference should be close to zero, except where reservoir changes have occurred. However, the subtraction process exhibits residual energy, which is not related to the time-lapse signal such as random noise, different acquisition parameters, and signal bandwidth variation. This energy often limits the resolution of the 4D signal (Vedanti et al., 2009).

[1] The reader is referred to Claerbout (1971) for more details concerning imaging conditions.

Chapter 5

Results

5.1 Preprocessing

5.1.1 Source wavelet

In order to generate the source wavelet to be used as input for FWI, the far-field signature without ghosts was imported from PGS's Geophysical support as seen in figure 5.1 It was important that the imported far-field signature did not contain any ghosts, as the FWI would generate the ghosts in the forward modelling using the free surface. The far-field signature was then convoluted with a minimum phase filter, figure 5.2, to get a (casual) minimum phase wavelet, see figure 5.3. The filter generation was performed using PGS's software Nucleus+. For each frequency band in the inversion, the minimum phase wavelet was convolved with a Butterworth bandpass filter and resampled to 20ms, as seen in figure 5.4.

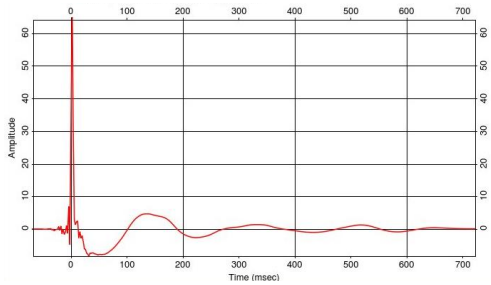

Figure 5.1: Far-field signature

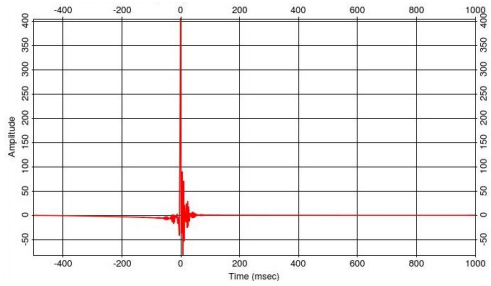

Figure 5.2: Minimum phase filter

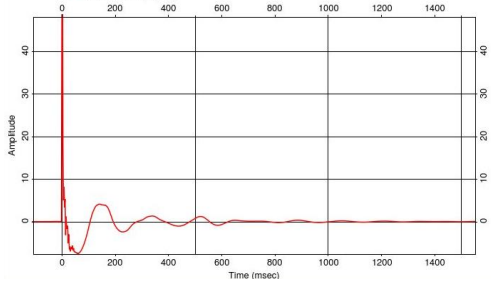

Figure 5.3: Far-field signature convolved with minimum phase filter

For the first frequency band, the Butterworth filter was set to 2-6Hz with slopes 36$dB/Ocatave$ and 72$dB/Ocatave$, see figure 5.4b. The final source wavelets are illustrated in in figure 5.5.

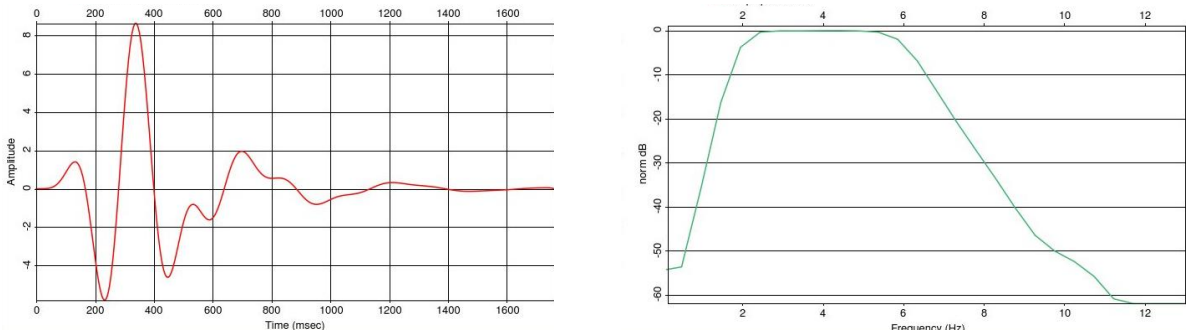

(a) Butterworth filter **(b)** Frequency specter for the Butterworth filter.

Figure 5.4: Bandpass filter

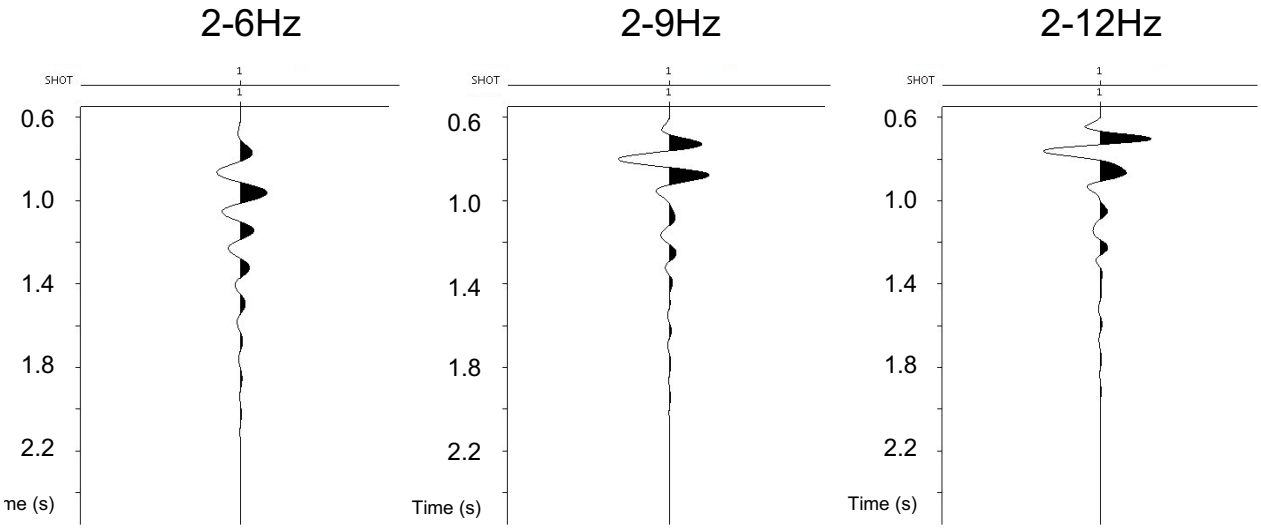

Figure 5.5: Generated source wavelets used as input for FWI.

5.1.2 Seismic

For the raw hydrophone data being used as input for FWI, some precondition was also necessary. The first step was to remove unwanted noise, as the noise would not be included in the forward modelling and hence the comparison with the real data would be difficult. The denoise

process included swell noise attenuation and linear noise removal, for example, tug noise, see figure 5.6.

Second, the same minimum phase filter as used for the source wavelet was applied to the hydrophone data. Then the third step was to limit the wavenumbers by applying the same bandpass filter as for the source wavelet. It was also important that the bandpass filter was minimum phased in order to keep the filtered wavelet and seismic data minimum phased.

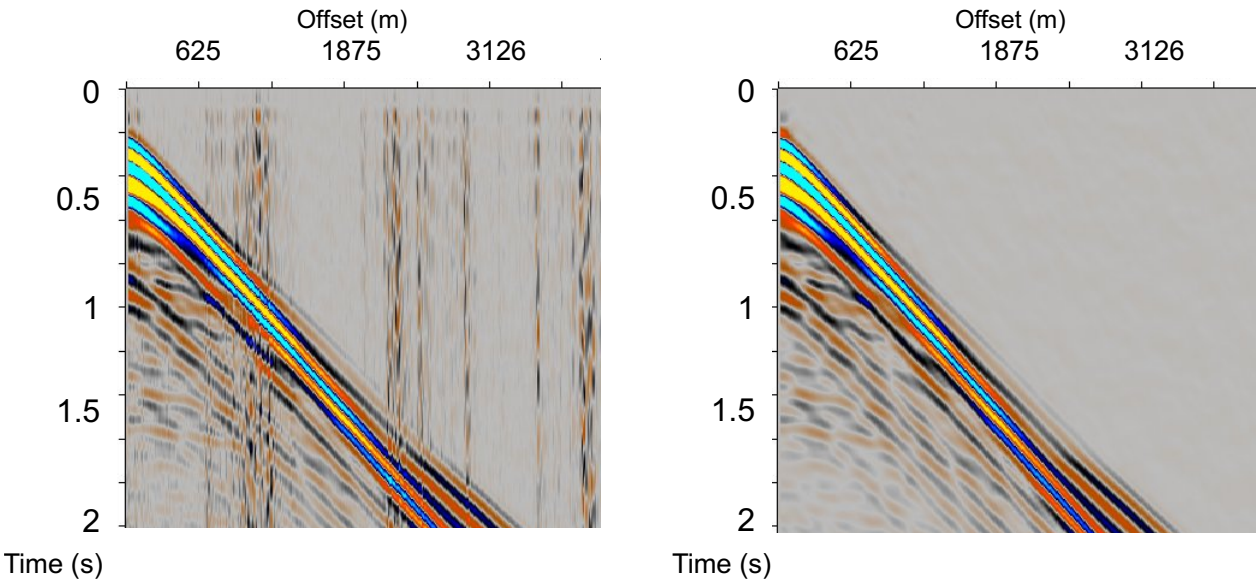

Figure 5.6: Before and after denoise. The left shot illustrates the shot before denoise and the right show after the denoise operation. The swell noise is visible as vertical noisy stripes.

5.2 Full waveform inversion

The FWI implementation used in this project relies mostly on refracted energy and diving waves. Reflected energy has also been tested in the inversion, but did not work as planned. As mentioned, the area of interest in this project is a shallow target, around 800-1000m depth, which makes FWI suitable. The velocity analysis procedure is based on the full wavefield modeling by iterative updating and minimizing the difference between observed and modeled seismic data. With an accurate velocity model of the Earth, it may provide more reliable seismic images to

interpret and gain more information about the gas saturation.

As described in chapter 5.1, generating source wavelet and data precondition was performed prior to the inversion. To reduce the computational cost of the inversion process, the data was divided into three different groups where every third shot was selected. By this method, the input shots were reduced from 6200 shots to 2066 shots and hence the computational cost was reduced by a factor of three (Ha and Shin, 2013). Three passes at each frequency band were then performed, so all shots were used.

For the inversion algorithm, the code was set to terminate when reaching 8 iterations or when the convergence criterion was satisfied, whichever happened first. The convergence criterion was set to 0.01 meaning that the inversion would terminate when the relative change in the objective function was 0.01 or less between the iterations. Consequently, the maximum number of iterations at each frequency band were 3 x 8 iterations. Constant anisotropy parameters were set to respectively 2% for delta and 3% for epsilon. Signal to noise ratio was investigated prior to the inversion to detect the lowest frequency band with high enough signal. We found that filtering the data to 2-6Hz would give high signal to noise ratio, this was therefore used as the first frequency band.

A header mute which followed the first break was applied to the input data, see figure 5.7. Then a taper parameter was set to 0.25 for the first pass, 0.35 for the second pass and 0.45 for the third pass. The parameter selects the amount of diving and refracted waves used in the inversion. By gradually increasing the parameter for each pass, more diving and refracted energy were used.

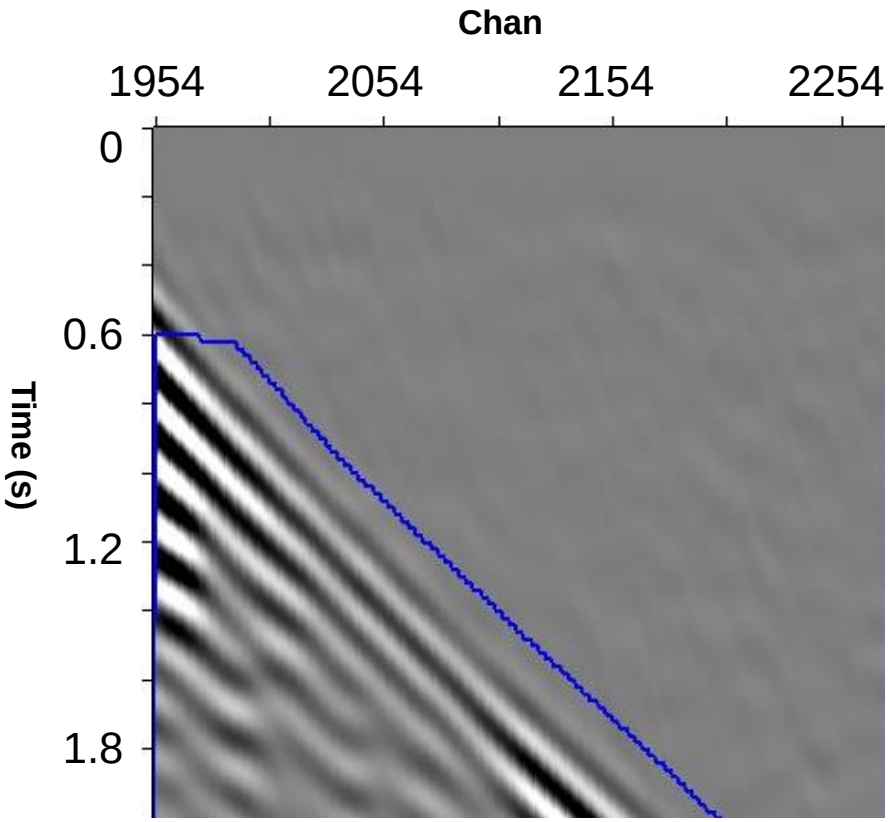

Figure 5.7: Input shot for FWI 2-6Hz. The shot is taken from the middle cable. The header mute is applied to the input shots for then to select the amount of refracted and diving waves used in the inversion.

For the first frequency band, on 2-6Hz, the initial starting model (figure 5.8) was used. For the next runs, the final model from the previous inversion run was used as input model. Before a new inversion process was initiated, several quality checks were applied. The fast Beam migration was performed after each pass with the updated model at that time. The QC migration outputs both stacks and offset gathers. Forward modelling shots within and outside the CO_2 plume were also constructed for each model update to detect cycle-skipping.

5.2.1 Initial model and forward modelling

No well-logs were available for this project, which could have given us an indicator of the subsurface velocities. Therefor, a model from another project was imported. The model covered the same area, but with increased lateral extent. The imported model was truncated and stacked so

no changes in lateral direction were present. The water velocity was $1490 m/s$, while the maximum velocity $2100 m/s$. The depth was set to $2 km$. The geological setting in the study area was mostly flat, which indicated that our simple starting model could be accurate as an initial model.

Different methods for verifying the initial model are described in the following figures. At first, forward modelling with the initial starting model was performed. The purpose with forward modelling is to confirm that the wavelet matches the observed data and confirm that the velocity model is close enough to initiate the inversion. As seen in figure 5.9, the forward modeled shots for 2-6Hz with the initial model show a good match for the first arrivals. The real shot is located within the gas plume.

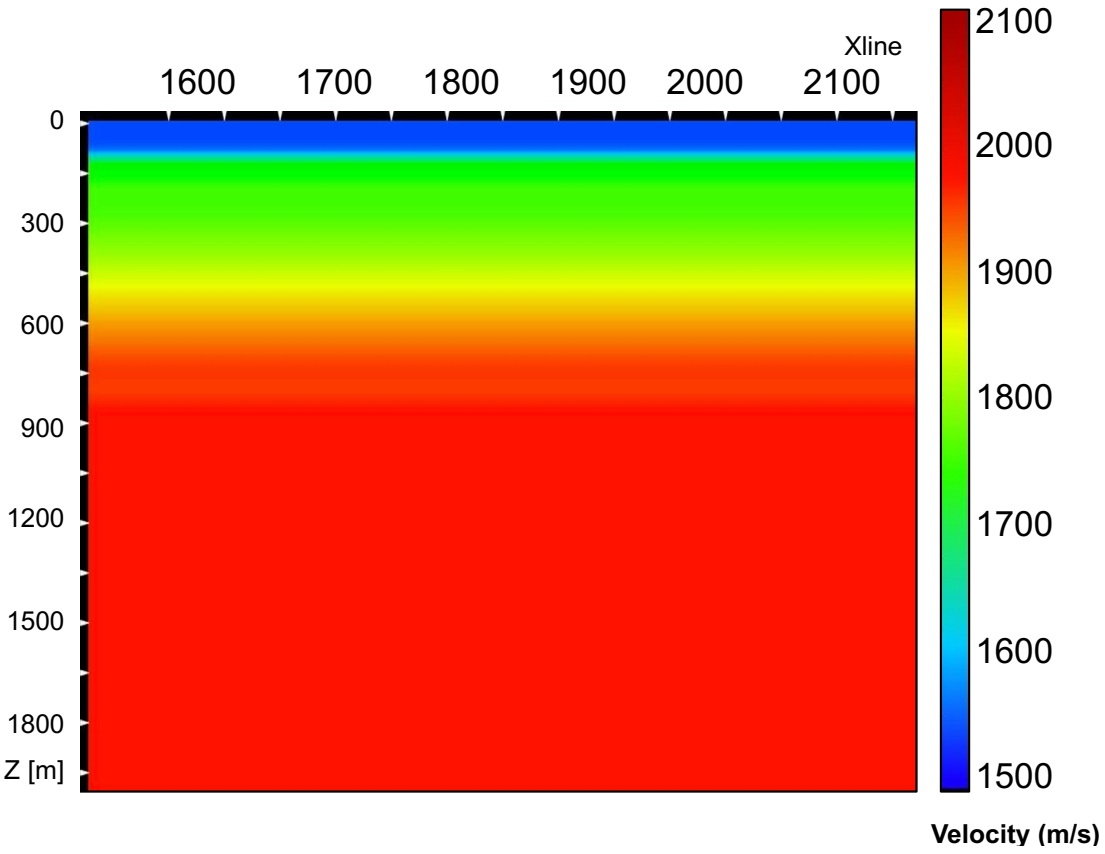

Figure 5.8: Initial velocity model.

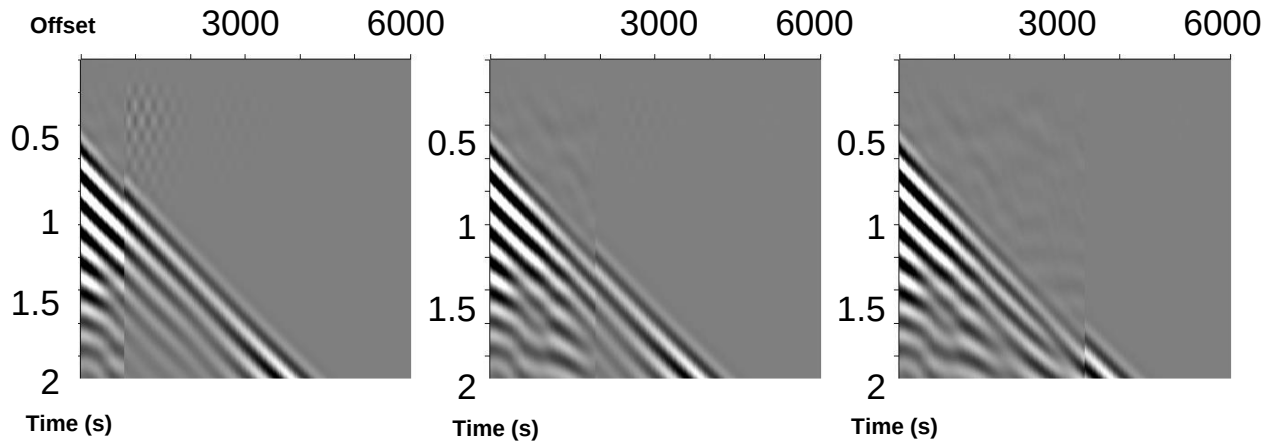

Figure 5.9: Comparison between modeled and observed shot. The three displays show the real shot to the left and the modeled shot to the right at different offsets. The modeled shots are generated with the initial velocity model. The real shot is located within the CO_2 plume.

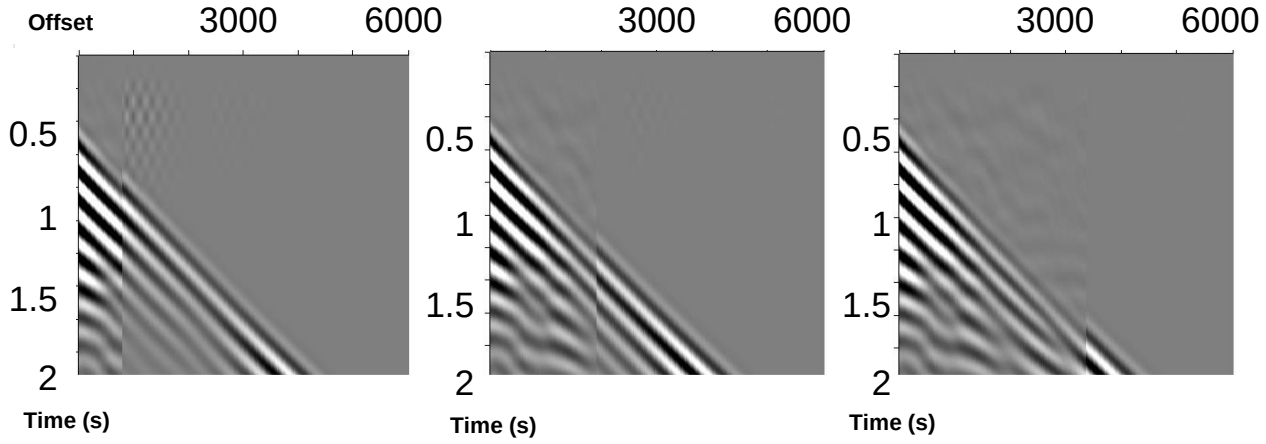

Figure 5.10: Comparison between modeled and observed shot. The three displays show the real shot to the left and modeled shot to the right at different offsets.The modeled shots are generated with the model after FWI 2-6Hz. The real shots are located within the CO_2 plume.

Analyzing the match between modeled and real seismic data is important with respect to cycle skipping. Events that are mispositioned more than a half cycle, may cause cycle skipping. To further evaluate the model, time shift maps were created to make sure the events were misposi-

tioned less than a half cycle. Time shift maps generated for the initial model and model created after FWI 2-6Hz show a reduction in time shift, especially at the far offset as seen in figure 5.11. The time shifts maps are calculated in the window from the mute header to the taper parameter. Several events in both real and modeled data will therefore be compared and average time shifts are calculated for each shot position.

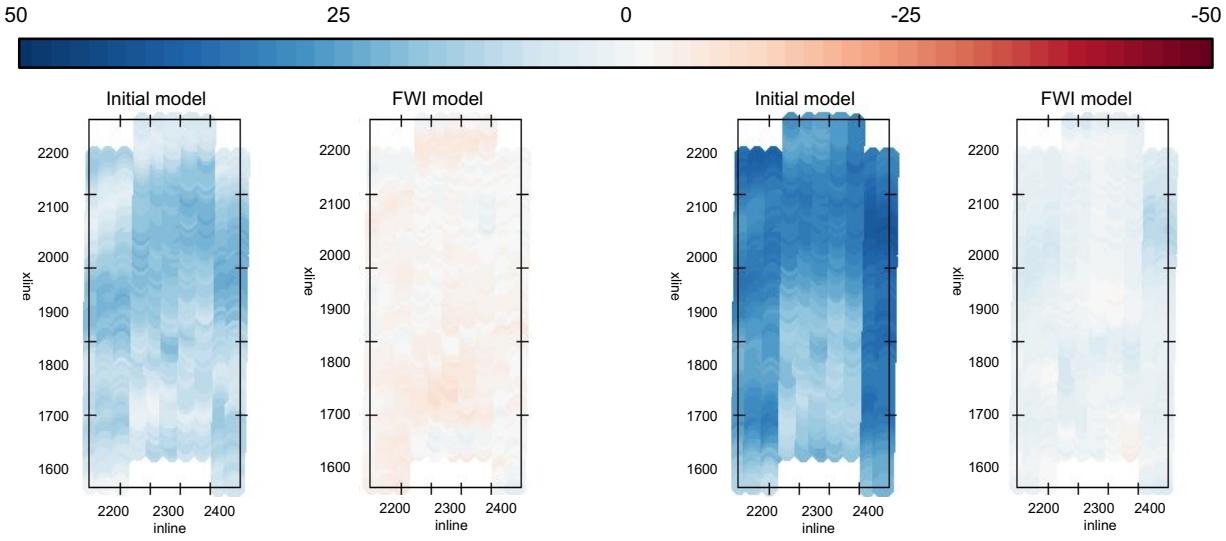

(a) Near offset. **(b)** Far offset.

Figure 5.11: Average time shift maps with the initial model and model created after first inversion on 2-6Hz.

The third quality check for the initial velocity model is seen in offset gathers computed from Beam migration, figure 5.12. With updated and hopefully more reliable velocities it was expected that the gathers would flatten. Comparing the gathers with the initial velocity model (figure 5.12a) and model created after the first inversion (figure 5.12b), the updated model improved the flatness of the gathers.

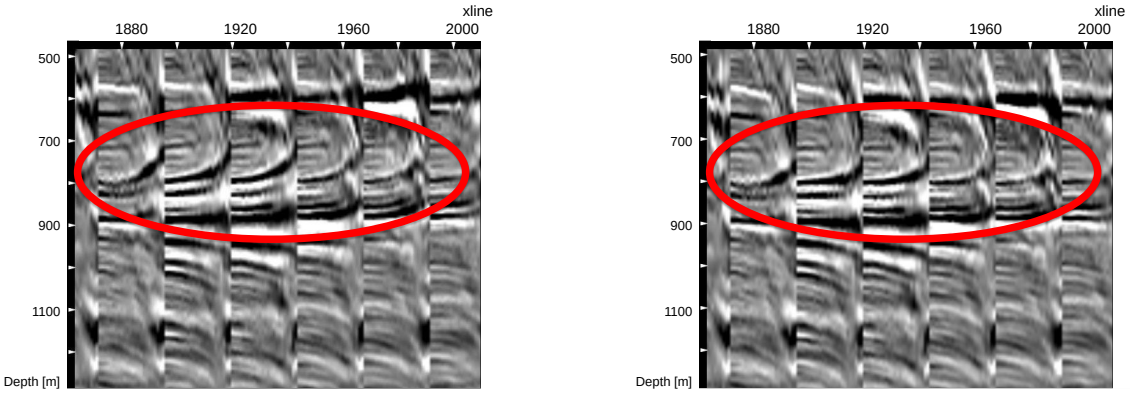

(a) Initial starting model

(b) Updated model after first inversion pass

Figure 5.12: Gathers with the initial model and the model created after the first inversion on 2-6Hz. Note the flattening of the moveout on the events within the red circle. These events are from the gas bearing layers.

After four iterations of inversion with the initial velocity model for 2-6Hz the misfit had decreased to 63 percent as plot 5.13 shows. The inversion was killed after 5 iterations because the misfit started to increase. There can be several explanations why the misfit did not converge. The initial model may have been too far from the reality and so the inversion starting point would not have been "in the flanks" of the global minimum. The step length may have been too big, but by decreasing the step length the inversion would require more iterations and hence the cost increase. Other parameters could also have been changed, such as the bin size or how much smoothing applied to the gradient. Due to time limitations, we continued with this result.

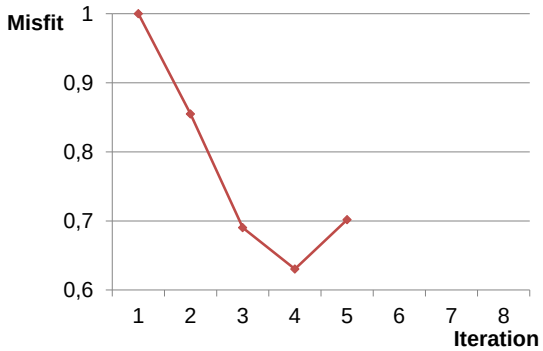

Figure 5.13: Misfit function from FWI with initial model.

The updated velocity model after these four iterations was then used for the next pass. The

result after this inversion is shown by the misfit curve in figure 5.14. The fact that the misfit was again decreasing was promising for further work.

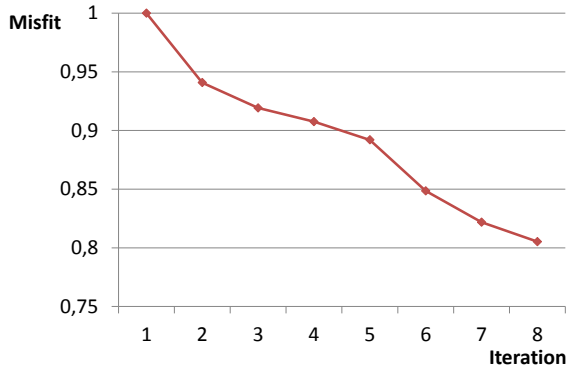

Figure 5.14: The misfit function with the updated model after first pass. Note that the misfit measure is normalized and will therefore always start at 1 for the first iteration. This means that since the job is restarted, the curve is not continued.

With the observed development described in forward modelling, reduction in time shifts and the improved gather flatness, it was decided to increase the frequency band for FWI.

5.2.2 High frequency velocity model

When the first three passes for 2-6Hz were completed, the frequency band was increased to 2-9Hz and then 2-12Hz. The figures below show the results and different quality checks for each frequency band.

Figure 5.15 shows the development of time shifts after FWI for 2-9Hz. After three passes of FWI the time shifts had reduced significantly on the near offset (figure 5.15a). On the far offset on the other hand (figure 5.15b), little change was visible.

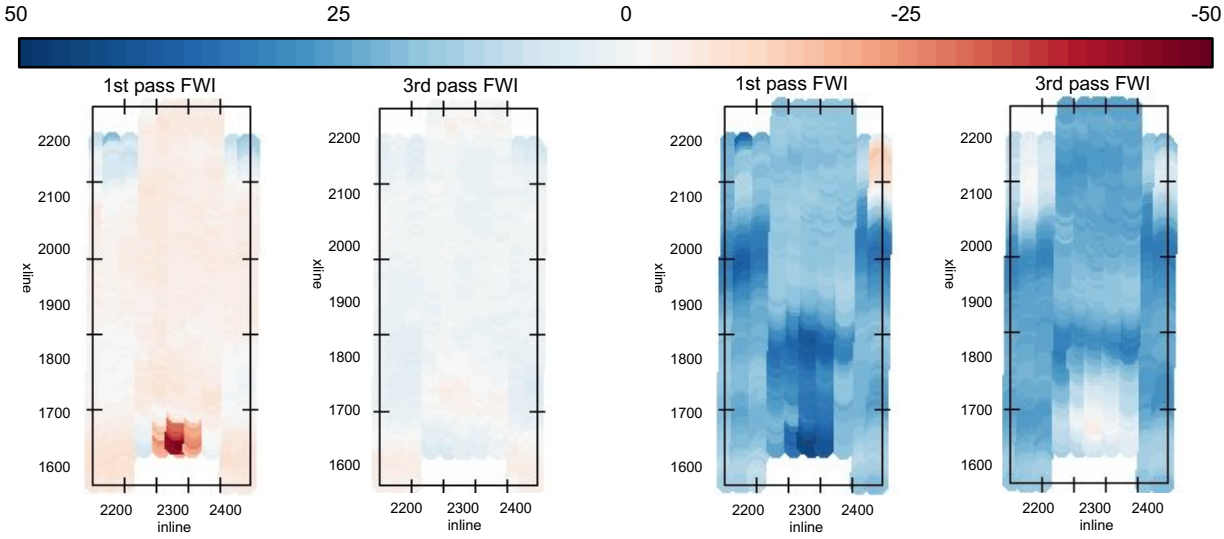

(a) Near offset. **(b)** Far offset.

Figure 5.15: Time shift maps 2-9Hz.

The time shifts observations were also visible in the comparison between real and modeled shots, see figure 5.16. On the near offset, the first arrivals seemed to fit well with the real data, but at the far offset a small time shift was visible. Nevertheless, we believed we were avoiding cycle skipping.

The updated model after inversion 2-9Hz is compared with the initial starting model in figure 5.17. Here a depth slice at 240m shows velocity changes in the updated model. By interpreting the seismic depth slice, figure 5.17c, it is clear that the updated model, figure 5.17b, follows the channel-like features observed in the seismic. The sediments deposits within the channels show lower velocities than the surrounding.

When observing the differences between offset gathers with the model after FWI 2-6Hz and 2-9Hz, more flattening is observed with the updated model, see figure 5.18. Looking closer at the gathers in figure 5.18c and 5.18d, the moveout is reduced with the model after FWI 2-9Hz.

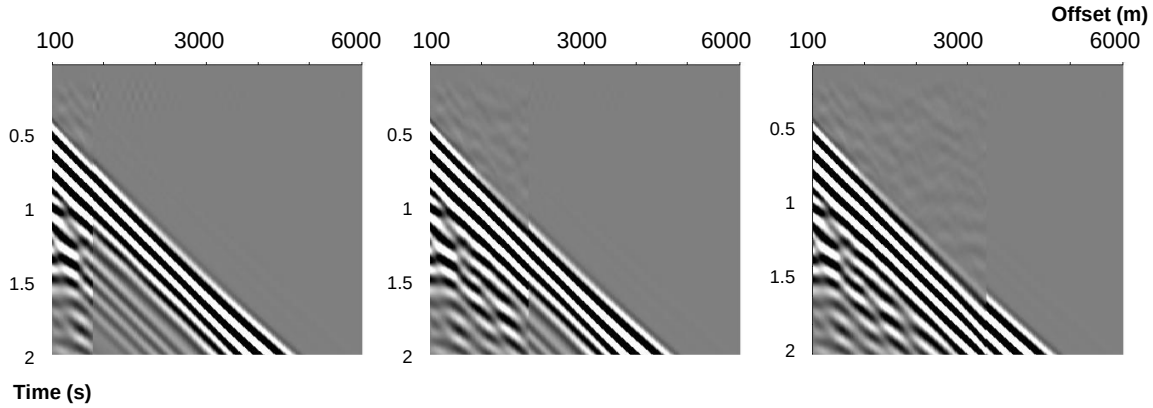

Figure 5.16: Real versus modeled shots on 2-9Hz at different offsets. Real shot to the left and modeled shot to the right.

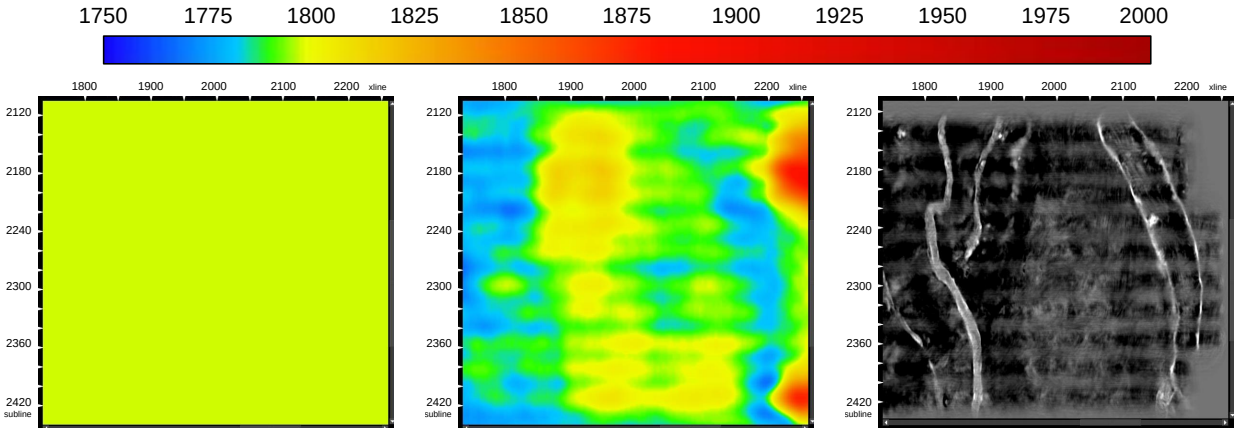

(a) Initial model **(b)** Model created after FWI 2-9Hz **(c)** Seismic

Figure 5.17: Depth slices at 240m for the for the initial model, model created after FWI 2-9Hz and the seismic alone, see figure B.1 in appendix for xline and inline location. Note how the updated model follow the channel-like features seen in the seismic.

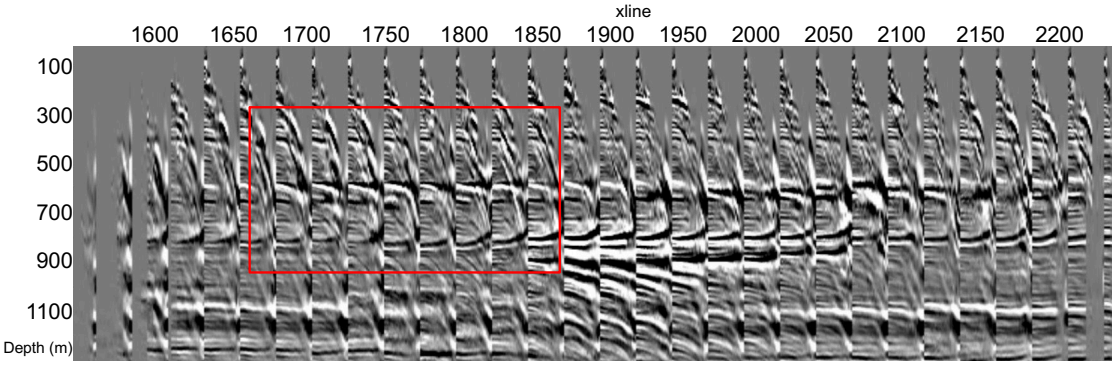

(a) Offset gathers with model created after FWI 2-6Hz.

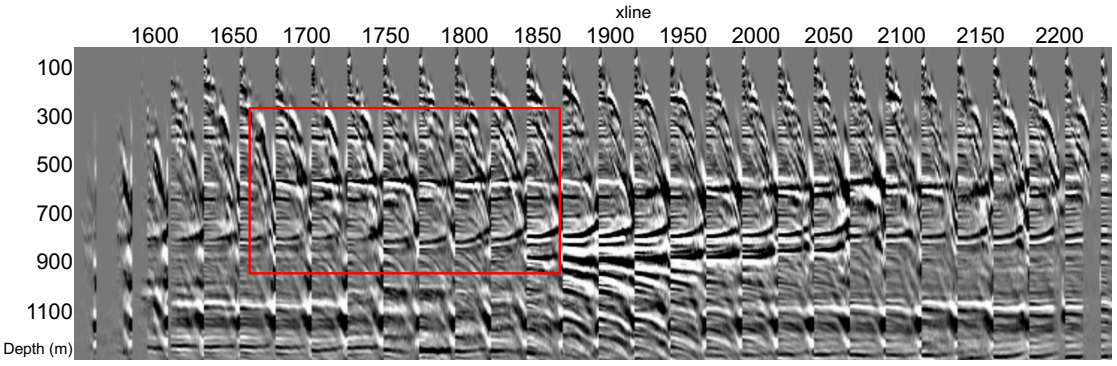

(b) Offset gathers with model created after FWI 2-9Hz.

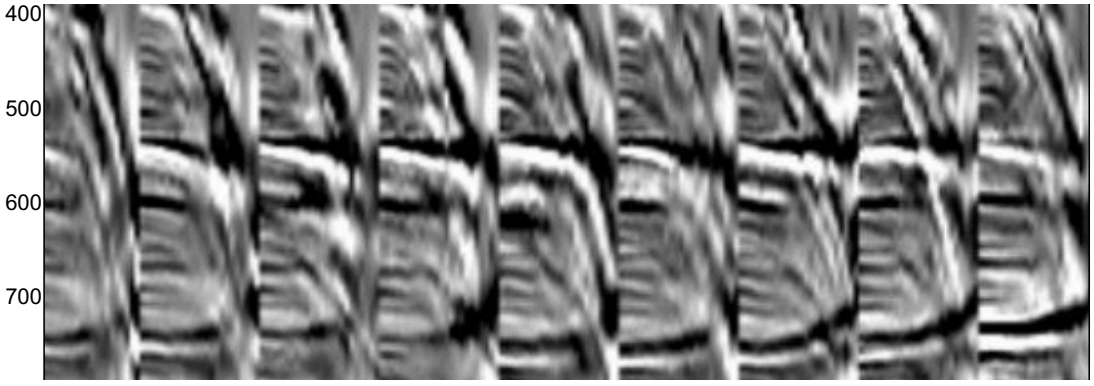

(c) Close up to the red rectangle in **(a)**

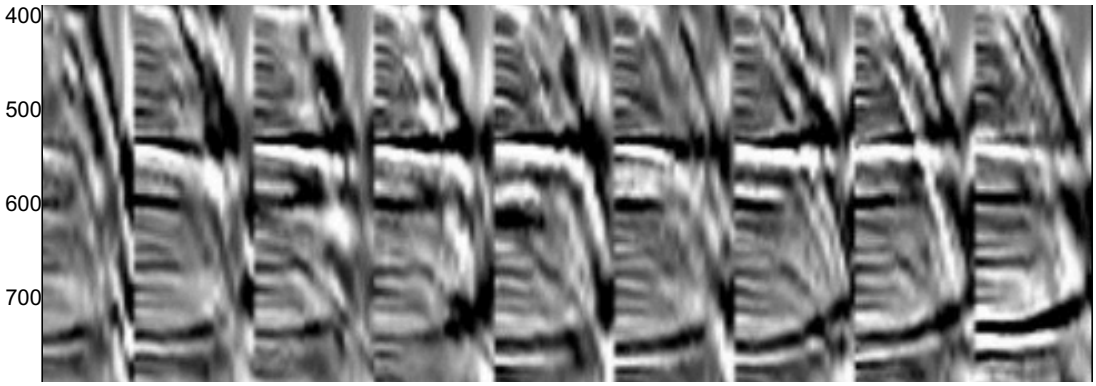

(d) Close up in to the red rectangle in **(b)**

Figure 5.18: Comparing offset gathers with the models created after FWI 2-6Hz and 2-9Hz, more correct velocities are observed in the shallow with the 2-9Hz model. The events around 550ms were getting more flat with the updated model.

When increasing the frequency band again, now up to 2-12Hz, the time shift maps show variable results. On the near offset, some time shifts almost completely disappear, while in other areas the time shifts actually increase after the third pass. This development was not desired. Little change in time shifts was visible at far offset.

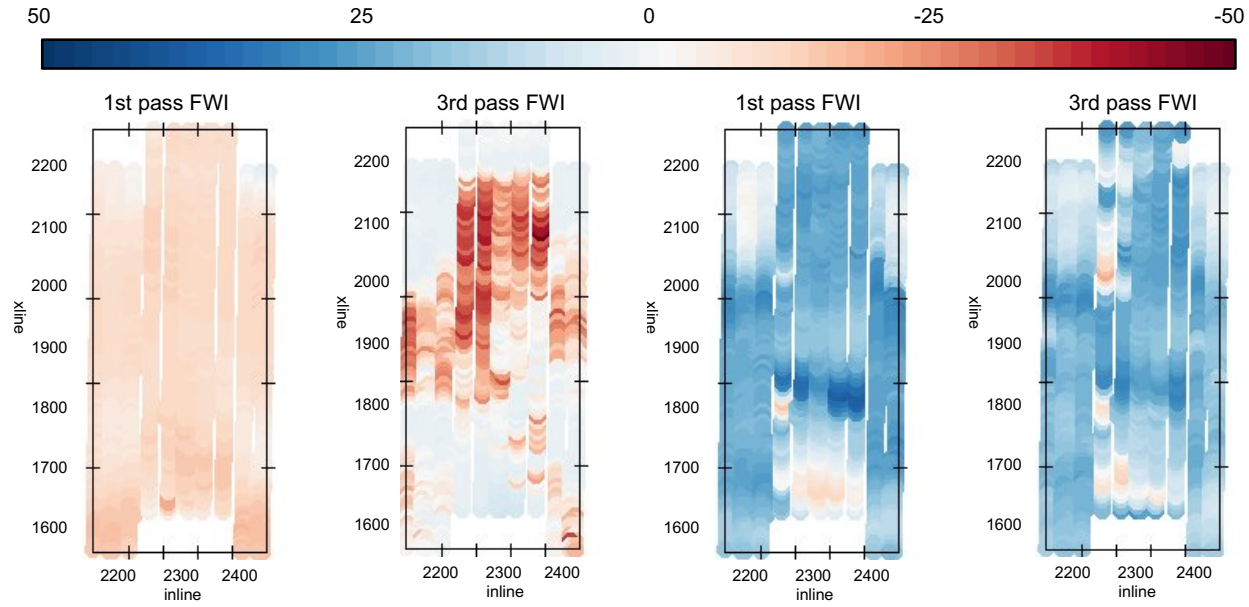

(a) Near offset. **(b)** Far offset.

Figure 5.19: Time shift maps for FWI 2-12Hz.

As the frequency band was increased, more events were visible in the shots. From figure 5.20, real versus modeled shots were compared. The real shot is shown to the left and the modeled shot to the right. Even though the time shift maps (figure 5.19) show a strange development, the modeled shots seemed to fit well with the real shots in the first arrivals.

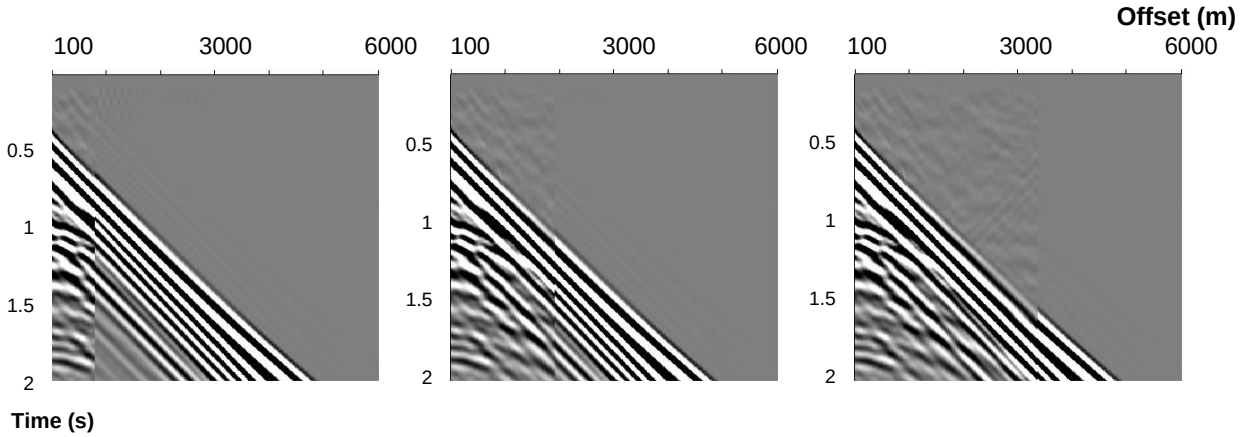

Figure 5.20: Real versus modeled shots on 2-12Hz at different offsets. Real shot to the left and modeled shot to the right.

The four models so far are seen in figure 5.21. Note that the vertical axis only goes from 300m and down to 1150m in the figures. The vertical slices are taken from inline 2264 which goes through the gas plume. What we from here on call the background model, is the model created after FWI 2-9Hz. We chose this model as the background model based on the undesired development in the 2-12Hz inversion and other quality checks just presented. Figure B.3 in appendix shows the same models at the same location with seismic overlaid.

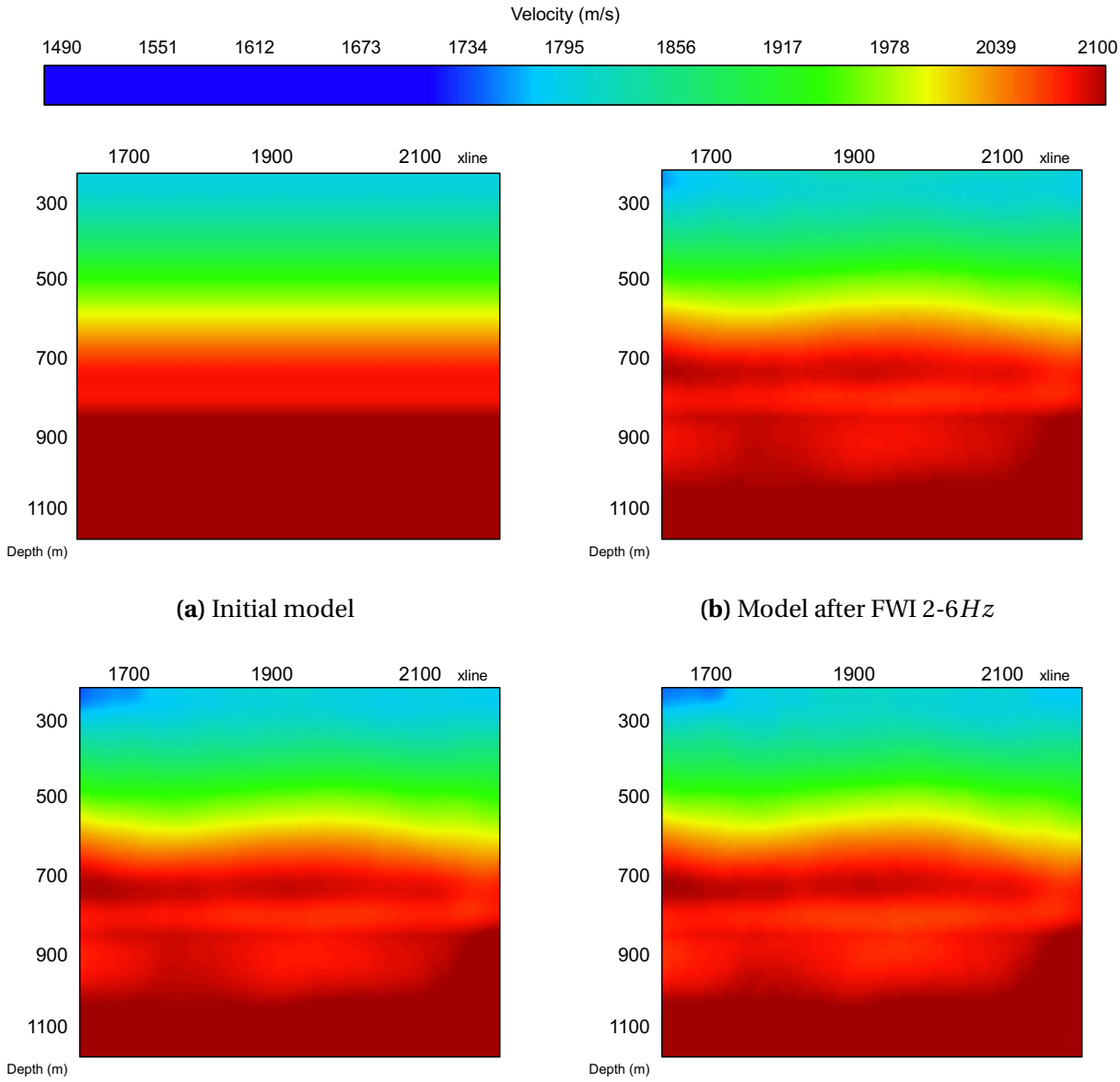

(a) Initial model

(b) Model after FWI 2-6Hz

(c) Model after 2-9Hz

(d) Model after 2-12Hz

Figure 5.21: Vertical slices for the different models at inline 2264.

5.2.3 Colored inversion

To include the low velocity in the CO_2 in the model, colored inversion was performed, limiting the velocity updates to the gas plume only. The colored inversion was applied to the background model. By lowpass filtering the seismic down to 0-9Hz, the gas layers stood out together with

other large amplitude contrasts in the data, see figure 5.22. By creating a gas mask, including only the gas saturated layers, several models were created by scaling the velocities within the mask. This means that the final model has the exact same values as the background model, but the low velocity gas layers were now included. The effect of the different models was studied with Beam migration and other quality checks. The model which had the best result was further used. The final model is shown in figure 5.23. The lowest velocity in the CO_2 layers in the final model was set to 1700 m/s. Note, the small lump to the left of the gas cloud in the final model should not have been included. This lump has nothing to do with the gas, but was discovered too late. The lump may cause unwanted migration and time-lapse results to be aware of.

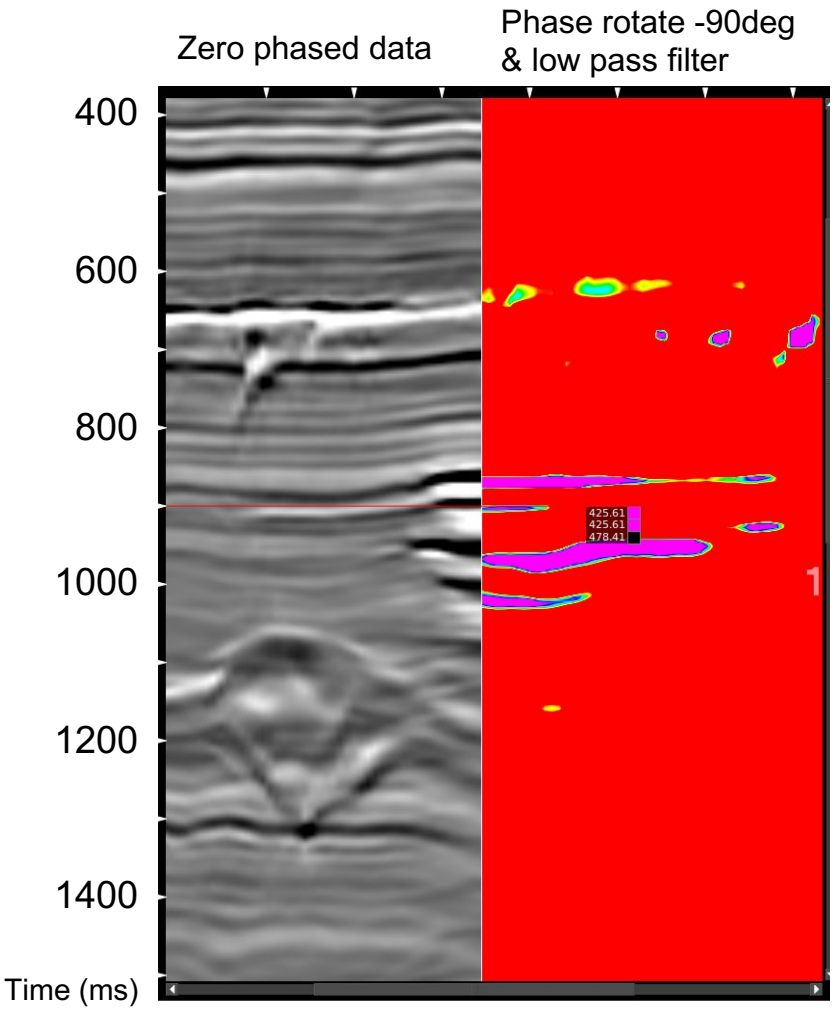

Figure 5.22: By lowpass filter and phase rotate -90^o it was possible to isolate several layers of gas in between trough (top gas) and peak (base gas).

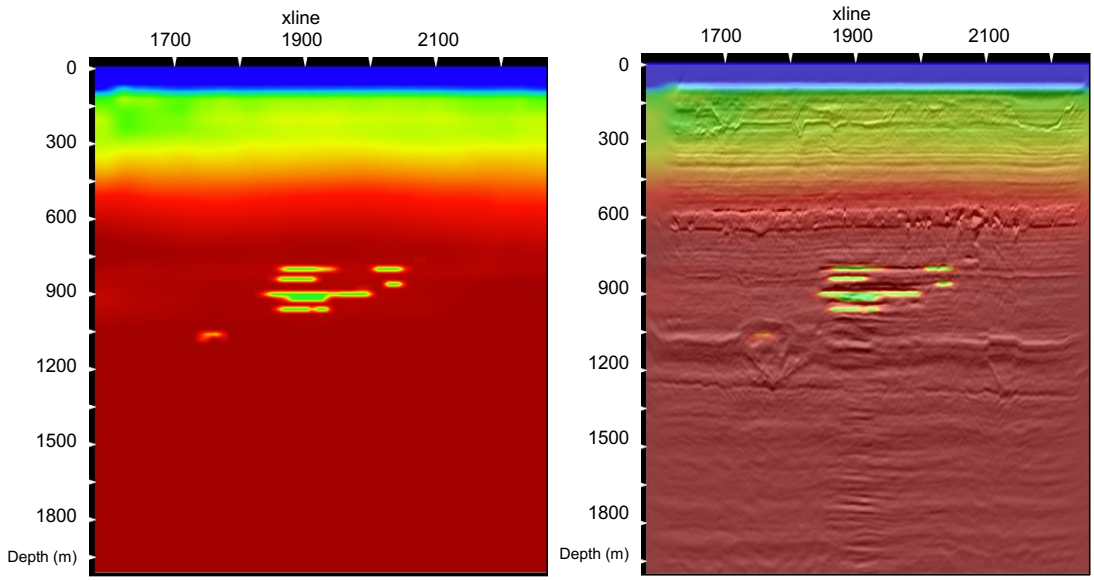

Figure 5.23: The final model created from colored inversion. Both profiles are taken from inline 2264. To the right, model with seismic overlaid.

Figure 5.24 shows the initial starting model, background model and the final model with the gas included at inline 2264.

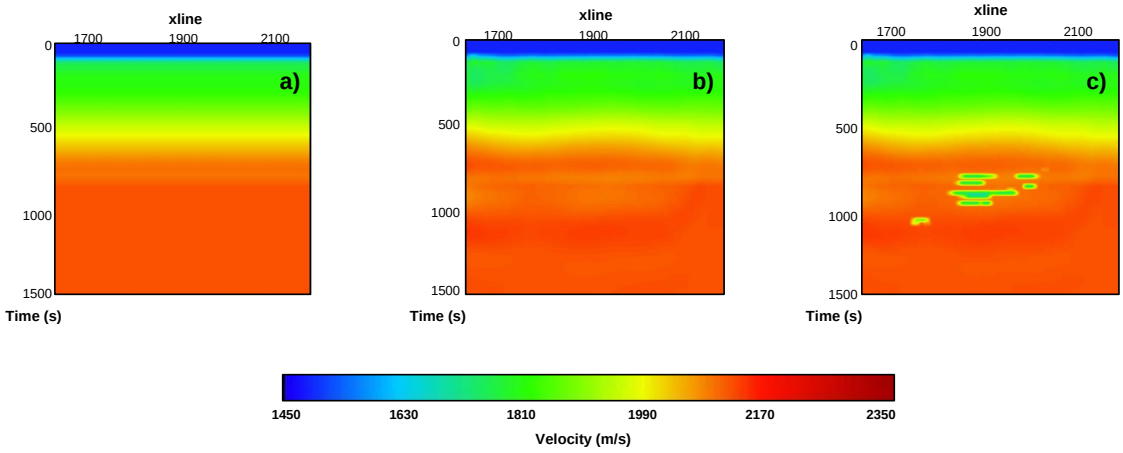

Figure 5.24: a) Initial starting model, **b)** background model, **c)** final model. All models are seen from inline 2264. The background model and final model have exactly same values, except in the included CO_2 layers in the final model.

Depth slice at 900m of the initial starting model and final model are shown in figure 5.25. This depth represents the depth where the CO_2 plume is located (see figure B.1 in appendix for xline

and inline locations). With these two models, Beam migration was performed and offset gathers are seen in figure 5.26. The bright events in the middle of the gathers are reflections from the gas plume itself. It is clear, especially at these events that the final model made the gather flatter. Note that the gathers are showing all incidents angels and hence moveout due to anisotropy may occur.

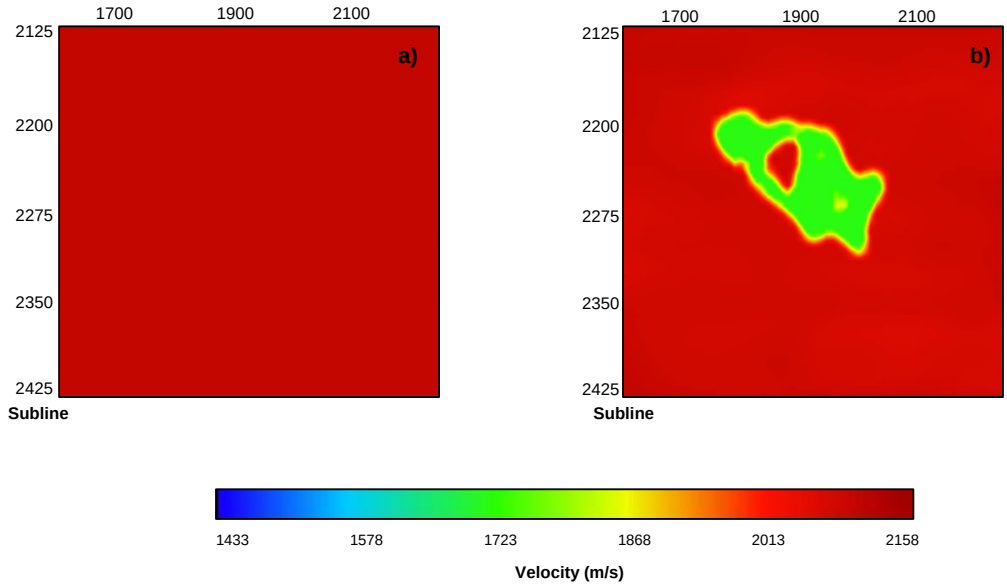

Figure 5.25: Model depth slices from 900m depth. **a)** Inital starting model, **b)** final model.

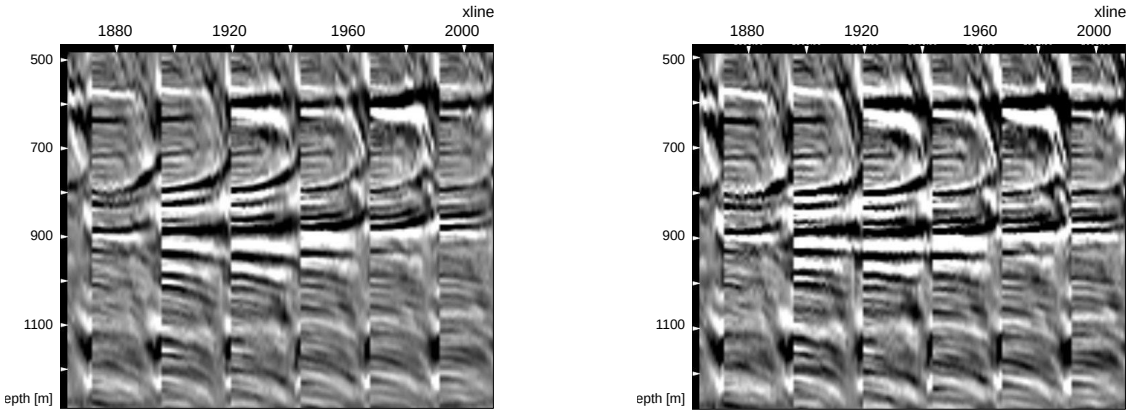

(a) Migrated with the initial model

(b) Migrated with the final model

Figure 5.26: Gathers from Beam migration.

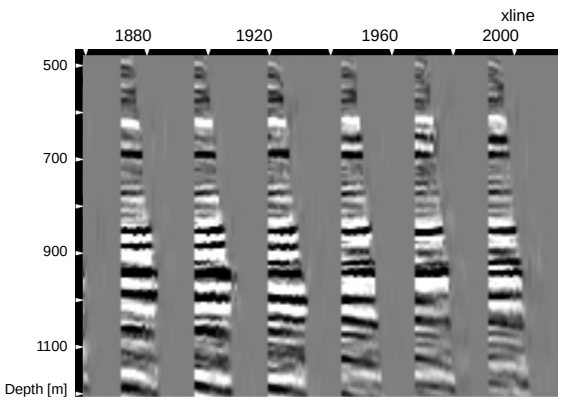

Figure 5.27: Gathers migrated with the final model and cut with angel of incident 0-35^o.

Now, when the final model included the gas, forward modelling was performed to see if we could get a good match with the observed data. If the modeled shots fitted well and the match did not show any cycle skipping, the final model should then be used as input to FWI. As seen in figure 5.28 the modeled shots were now for the first time able to include the "gas reflections". But by comparing the modeled shots to the real shots, the mismatch was obvious, see figure 5.29, so further inversion was not performed.

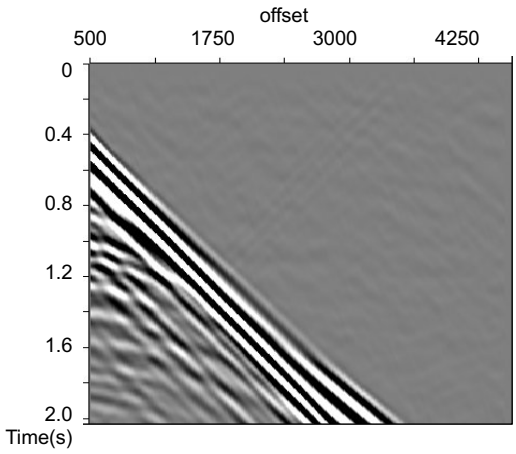

(a) Observed shot

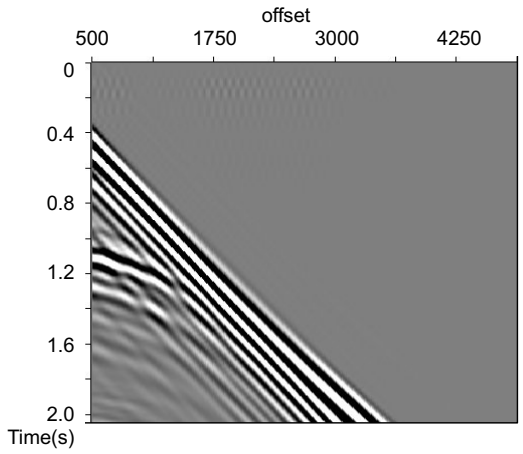

(b) Modeled shot with colored inversion model

Figure 5.28: Real shot from the gas cloud to the left and modeled shot to the right. Note the clear gas reflection in the modeled shot.

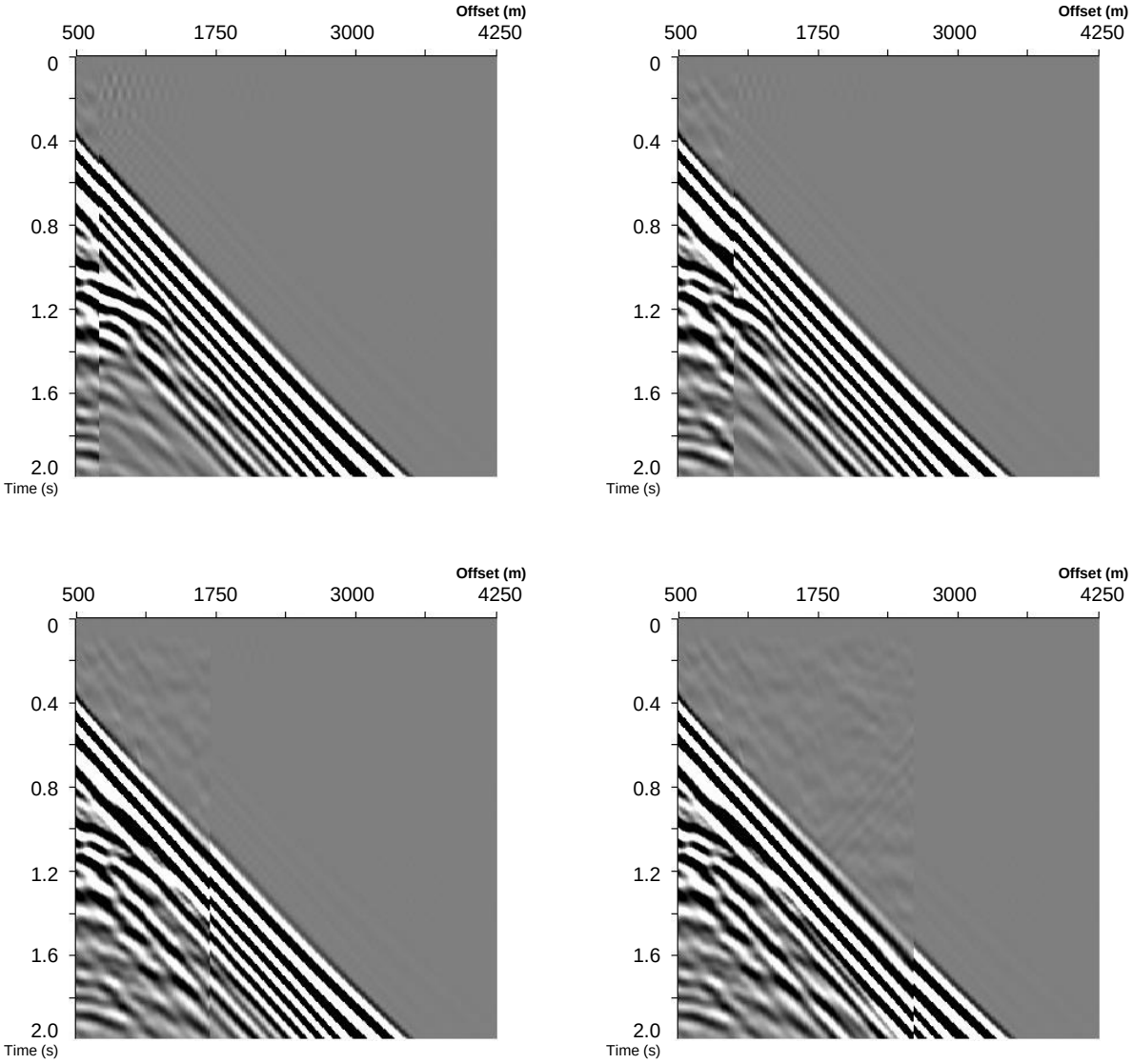

Figure 5.29: Real verses modeled shots at different offsets. The real shot is taken from the gas cloud. Gas reflections are visible in both real and modeled shots, but the mismatch is notable.

With this, we continued with the background model and colored inversion model (final model) for migration.

5.3 One-way wave equation migration

With the background model and the final model, WEM was performed on the surveys. First WEM with $40Hz$ was constructed, then with $80Hz$. For the base survey, the migration was only constructed using the background model since this model did not contain the CO_2 velocities. The results for the base survey are showed in figure 5.30. The image is from inline 2264 which goes through the gas plume. Note the horizon at $1250m$ depth (indicated by red arrows) which is fairly flat all over this inline. Further investigation of the rest of the volume showed the same flat horizon trend. This flat horizon was further used as a quality check for the migration of the monitor data.

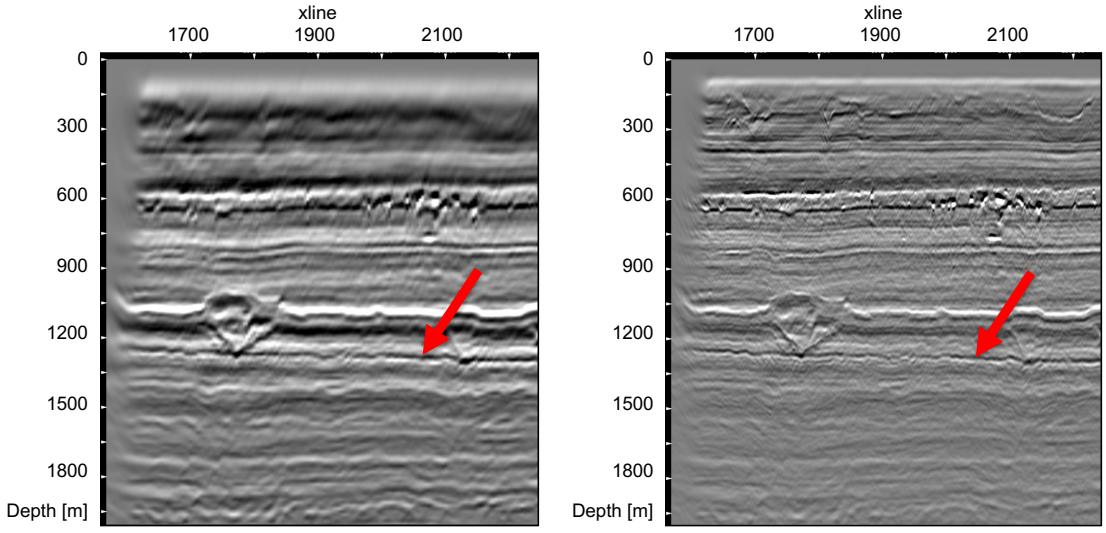

Figure 5.30: Results from wave equation migration for the base survey. Both images are migrated with the background model. $40Hz$ to the left and $80Hz$ to the right. The red arrow indicates a flat horizon which will be used as a quality check for the monitor data.

WEM with both models with $40Hz$ on the monitor data is showed in figure 5.31. Migration with the final model (right image in figure 5.31) makes the CO_2 layers thinner as well as flatter compared to the result from the background model (left image in figure 5.31) indicating that the final model was more representative of the real subsurface geology.

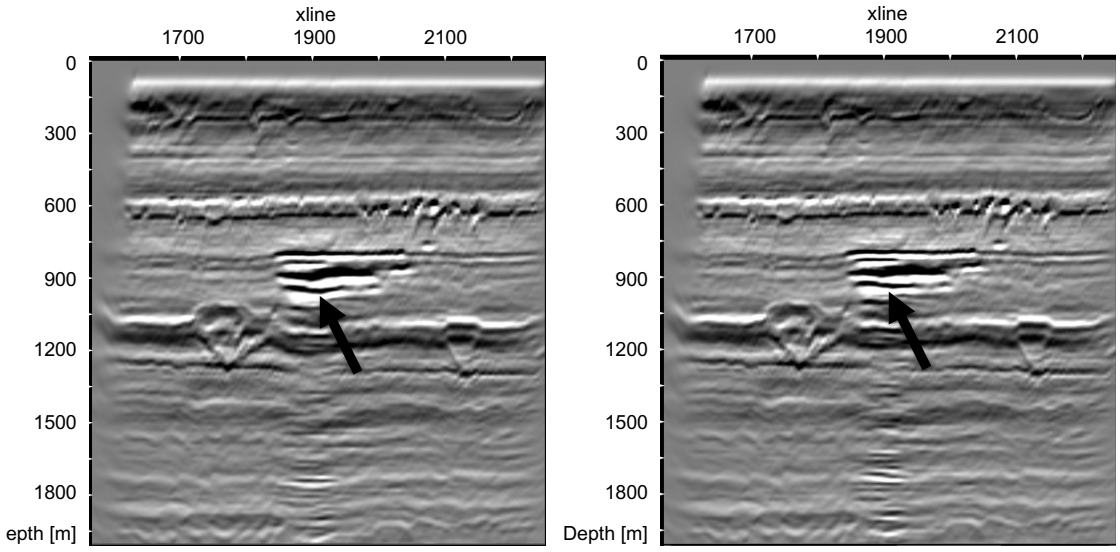

Figure 5.31: Results from WEM with an upper limit at $40Hz$ for the monitor survey. The image to the left was migrated with the background model, while the image to the right was migrated with the final model. The arrow indicates one layer which was flatter with the final model. Images are taken from inline 2264.

When increasing the frequency to $80Hz$, the same results were observed, see figure 5.32. Zooming into the zag in the horizon below the CO_2 at around $1250m$ depth, the layer appears flatter with the final model. Also, note that the CO_2 layers got thinner with the final model.

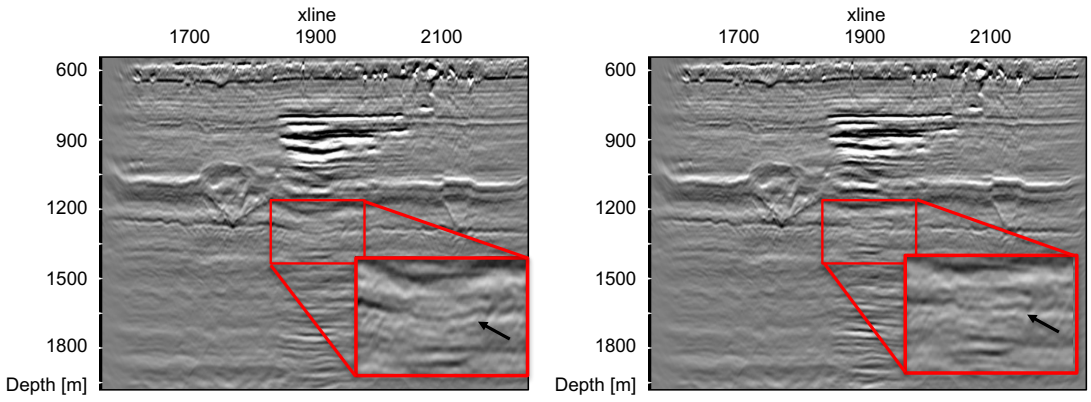

Figure 5.32: Results from WEM for the monitor survey. The migration was increased to $80Hz$ and more details got visible. The image to the left was migrated with the background model, while the image to the right was migrated with the final model.

Looking at depth $958m$ we are located in the lower part of the gas plume (see figure B.1 in ap-

pendix for xline and inline locations). Comparing this depth with the results from the WEM we observed a distinct difference between the seismic migrated with the background model and with the final model, see figures 5.33 and figure 5.34. What looks like a circularly shaped event with white edges and black core when migrate with the background model, has changed to just a white shaped event when migrated with the final model. By looking at the vertical slices the reason is obvious. For the seismic migrated with the background model (figure 5.33 to the right), the depth slice penetrates both positive and negative amplitudes. For the image migrated with the final model, the CO_2 saturated layers were more flat, and hence the depth slice cut through only positive amplitudes (figure 5.34 to the right).

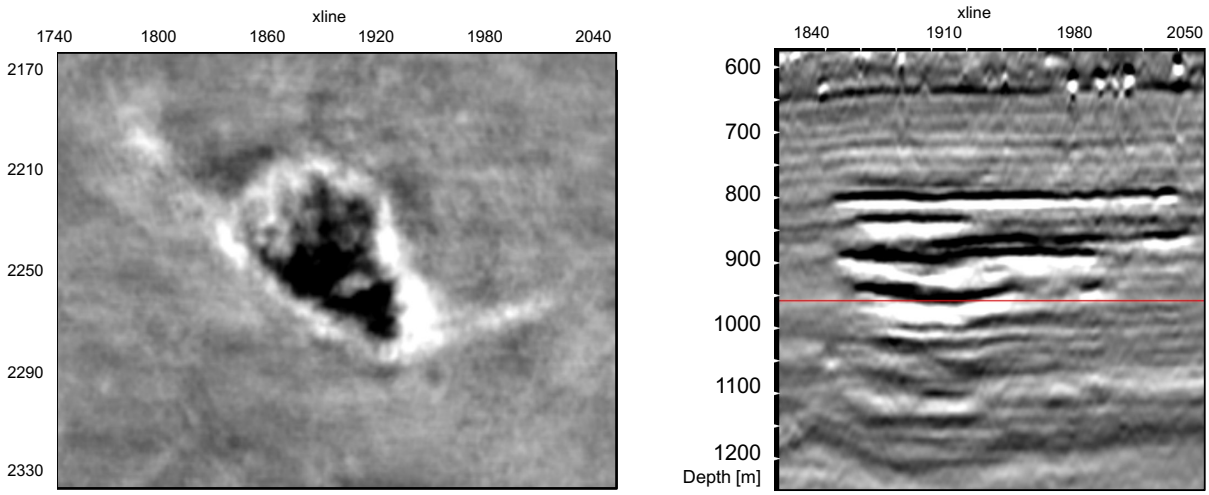

Figure 5.33: To the left: WEM depth slice at 958m for the monitor data migrated with the background model. To the right: location of the depth slice is illustrated with a red line.

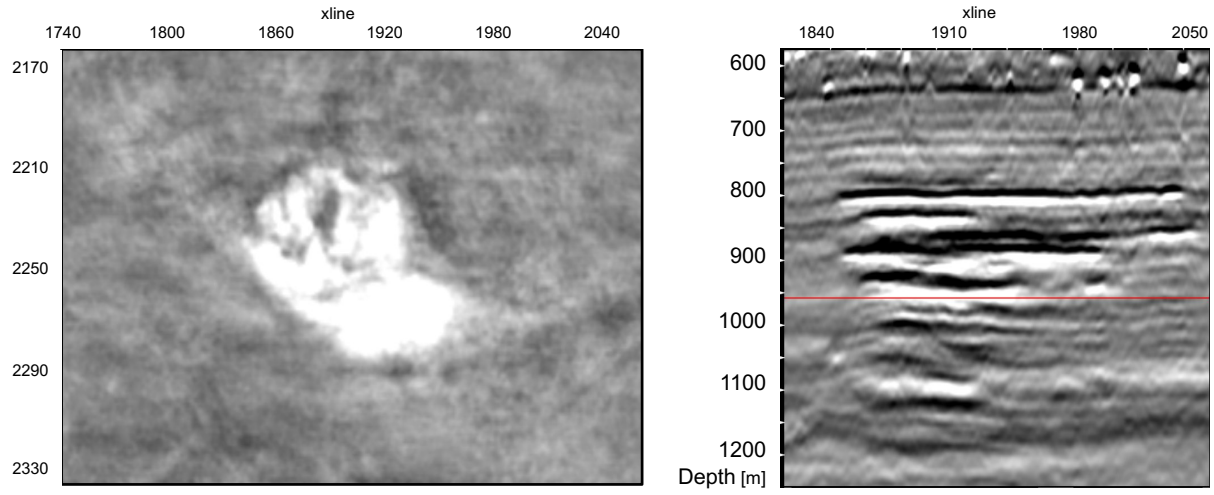

Figure 5.34: To the left: WEM depth slice at 958m for the monitor data migrated with the final model. To the right: location of the depth slice is illustrated with a red line.

From the base survey, migrated with the background model, we see the horizon below the gas injected was flat. Comparing the migration results for the monitor data we conclude that our final model did a reasonable good job for imaging the same horizon below the gas. The horizon was on the other side not flat when the monitor data was migrated with the background model. A clear zag was visible as figure 5.32 shows, indicating wrong velocities in the gas.

From the migrated data, we observed severe footprints oriented in the east-west direction as alternating weak and strong amplitude stripes. These amplitude stripes were related to acquisition geometry and not to geology. From the monitor data, the prominent acquisition footprints were visible especially in the shallow part, see figure 5.35. But as seen from figure 7.1 the sail line imprint was still visible at the target depth.

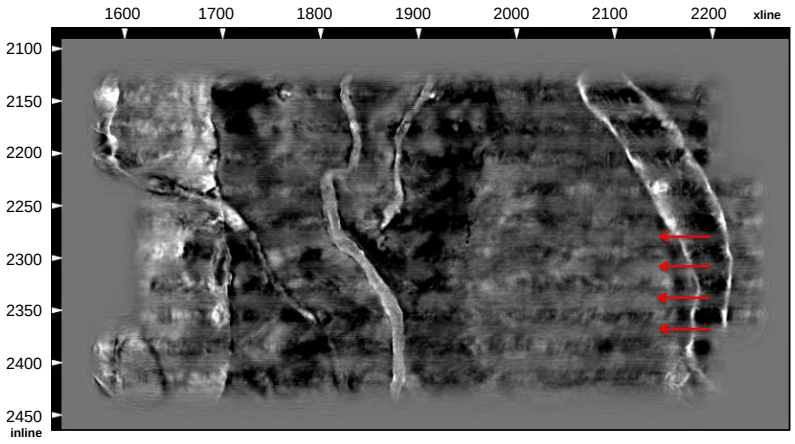

Figure 5.35: Depth = 240m. Red arrows indicate sail line imprints.

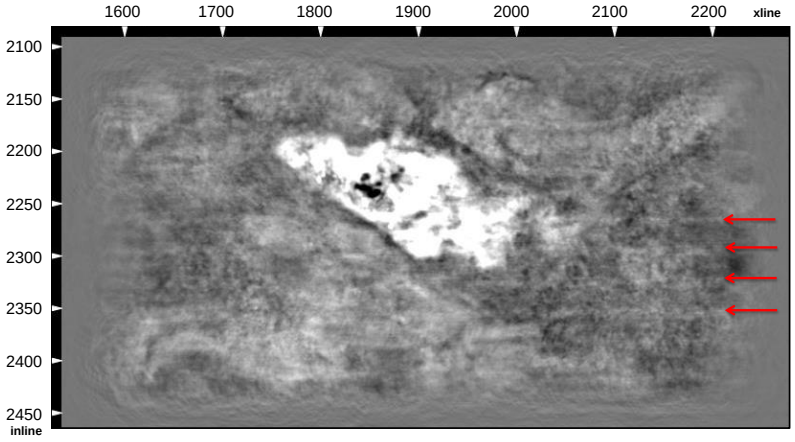

Figure 5.36: Depth = 900m. Red arrows indicate sail line imprints.

Figure 5.35 and 7.1: Depth slices over the Sleipner field with one-way wave equation migration. Sail line acquisition footprint seen as lateral stripes indicated by red arrows in the figures.

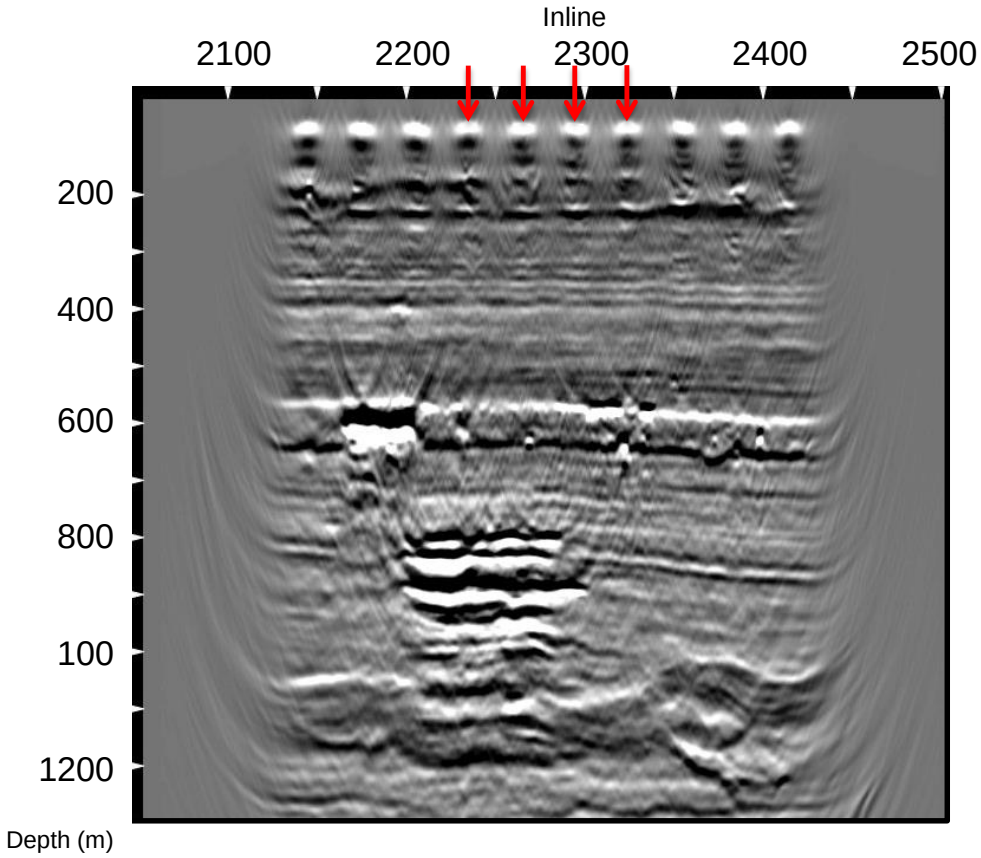

Figure 5.37: Acquisition footprint seen in xline profile. Xline 1900.

5.4 Time-lapse differences

For the time-lapse, the seismic after WEM was used. Since the WEM easily gets affected by acquisition footprints and remaining multiples, small artifacts in the migrated seismic may be magnified as a time-lapse response. Ideally, least-squares inversion should have been used on the migrated data before performing time-lapse [1]. The least-squares inversion would have attenuated uneven illumination artifacts related to acquisition and so the time-lapse response would not have been so affected by excessive 4D leakage. This is important to keep in mind when interpreting the time-lapse results.

In this study, proper 4D matching has not been done, but a simplified 4D matching was per-

[1] More about least-squares inversion in appendix A.3

formed prior to subtracting the monitor survey from the base survey. Average amplitude -, time shift - and phase shift differences between the two datasets were calculated in a small window (from top mute header to the taper parameter) and applied to the monitor data to get a better match between the datasets prior to the time-lapse study.

Figure 5.38 from inline 2264, shows time-lapse differences between the base survey and the monitor survey. In both profiles was the base survey migrated with the background model, while the monitor survey was migrated with the background model to the left and the final model to the right.

The CO_2 response itself was very clear, indicating strong confidence in the time-lapse observations. Note the strong time-lapse responses on the horizons below the CO_2 plume, seen in figure 5.38. These horizons were clearly affected by the low velocities in the plume, generating push down effects. No indication of high amplitude changes in the overburden above the gas plume were visible, and therefore no leakage of CO_2 had occurred. No time-lapse difference was observed at the top reservoir reflector, which was expected as the formation was unlikely to move (see figure 5.39). By zooming into the gas cloud, see figure 5.40, it was easier to detect the changes within the gas saturated layers. The uppermost red arrow indicates a CO_2 saturated layer which got thinner when the monitor survey was migrated with the final model. The next two arrows show layers that were curved with the background model, but straightened out with the final model.

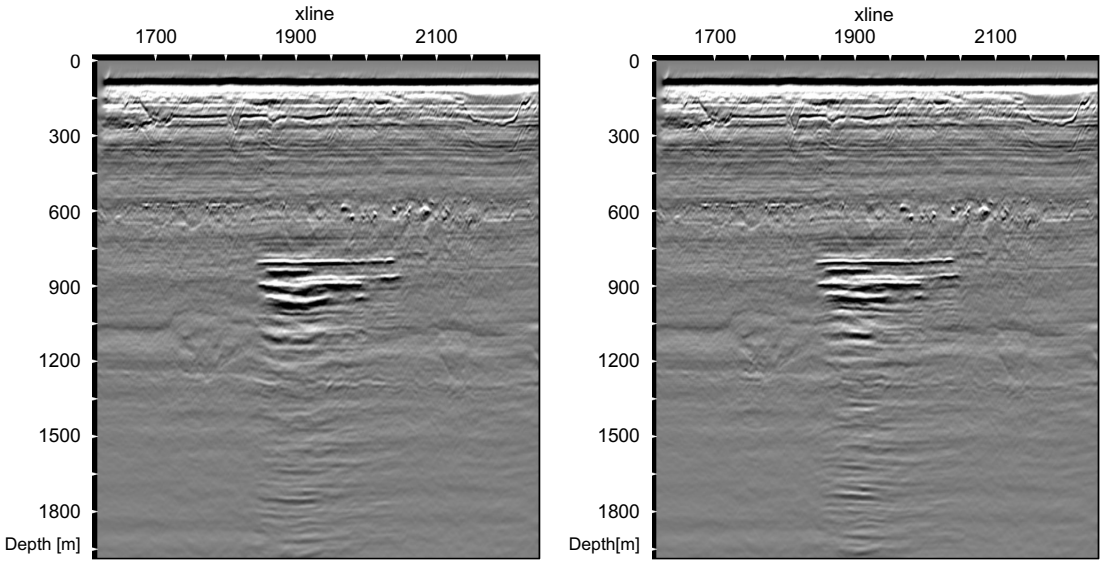

Figure 5.38: Time-lapse difference. Profile to the left shows time-lapse differences when both base and monitor survey were migrated with the background model, while on the profile to the right the monitor survey was migrated with the final model.

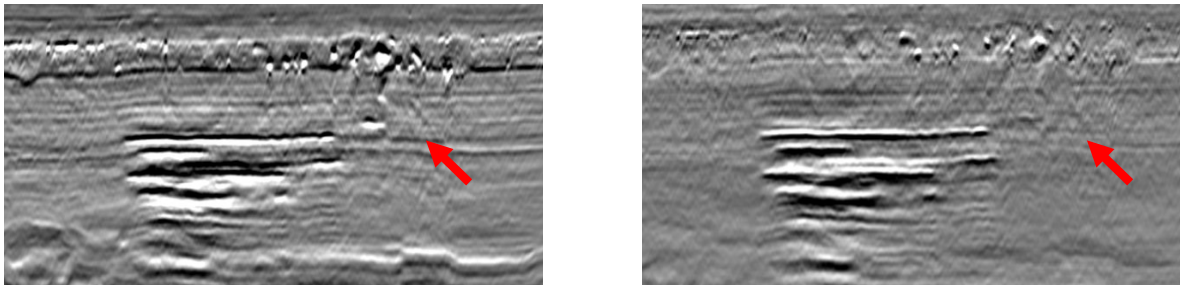

(a) Image after WEM

(b) 4D difference

Figure 5.39: As expected, the top reservoir horizon indicated by the red arrow in **a)** was not visible in the time-lapse response in **b)** .

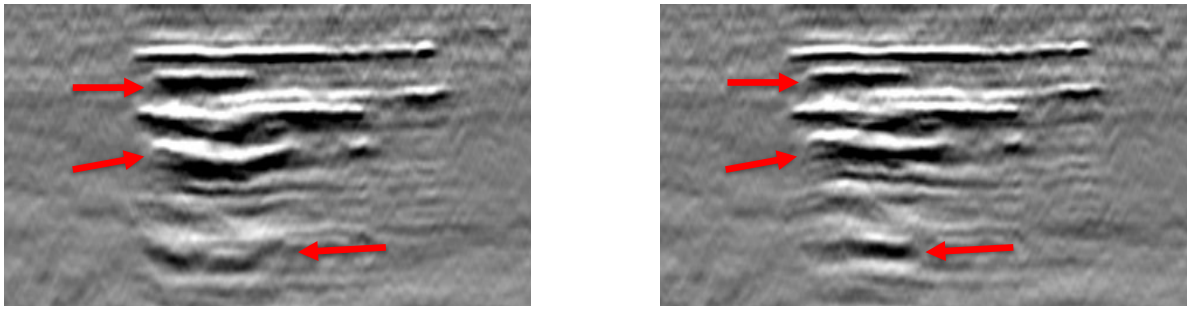

(a) Time-lapse difference where the monitor survey was migrated with the background model

(b) Time-lapse difference where the monitor survey was migrated with the final model

Figure 5.40: Time-lapse differences for the gas cloud. The red arrows indicate noticeable differences between the time-lapse results.

As mentioned, it is not ideal to use wave equation migration data for time-lapse studies. The time-lapse differences seen in the shallow part, might have been introduced by the weaknesses in WEM or by the different acquisition geometry for the two surveys.

In figure 5.41 several depth slices are shown for both 4D flows. Increasing the depth from 750m (which is just above the first gas saturated layers) down to 1000m, the gas layers are clear and strong indicating confidence in the time-lapse observations. The change in color for the two flows at same depth indicates that some events were being shifted with the different flows.

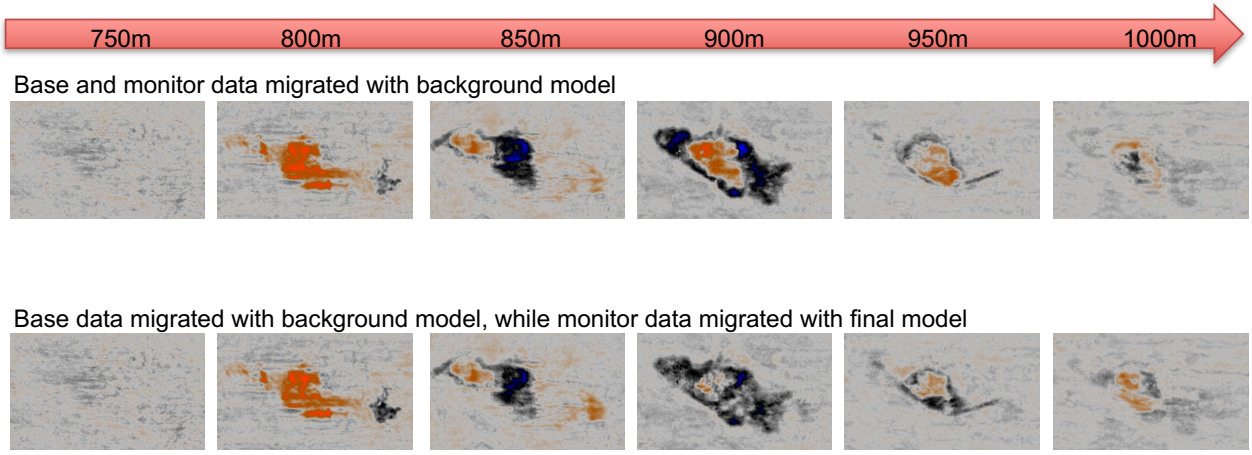

Figure 5.41: Time-lapse depth slices. In the first row, both base and monitor data were migrated with the background model, while in the bottom row, only the base data was migrated with the background model, while the monitor data was migrated with the final model. The red arrow indicates the subsurface depth.

Chapter 6

Discussion

6.1 Full waveform inversion

As mentioned in chapter 4, the velocity analysis in FWI is based on the full wavefield modelling and aims to estimate high-resolution velocity models, by minimizing the difference between observed and modeled data. As the initial velocity model will have great impact of how the misfit will decrease for each iteration, it is important that the initial model reflects the reality as closely as possible. Also, the initial velocity model should not have sharp interfaces or too many details. If the initial model is too far from reality it may cause cycle skipping and the inversion may be trapped in a local minimum instead of the global minimum. For this project, a smoothed 1-D velocity model with no lateral changes was used as the initial velocity model. No well-logs were available, which could have given an indicator of the subsurface velocities. Even though different quality checks of the initial velocity model showed that the model was suitable as a starting model, the model may have been too far from the reality. Introducing a low-velocity zone where the gas bearing layers were located, could have given us a better initial model. More time should have been spent on the starting model, but time limitations prevented this. Previously research has found that detailed velocity models from FWI can be used to extract geometry of gas clouds with high precision. On the other side, studies from the Sleipner Field have also showed that FWI struggles to update the low velocities in the gas (Raknes, 2015b).

There can be several reasons why the FWI in this project struggled to include the gas cloud in the models.

Firstly, the full waveform inversion in this project stopped at $12Hz$. At $12Hz$ reflections from the gas were barely visible. Only when increasing the frequency span up to 30-40Hz the reflections were getting clear and continuous. Without any clear reflections in the input data, the modeled shots will suffer and have problems to include this, and hence no update from the reflections will be included in the model.

Secondly, the velocity contrasts between the gas plume and the surroundings may have been too large and the layers too thin compared to what the FWI is able to handle.

The third possibility is related to the difference between the acoustic and elastic wave equation. In general, full waveform inversion uses the acoustic wave equation and not the elastic wave equation. The same approach for FWI was used in this project. Because the acoustic wave equation ignores the presence of shear waves, its implementation is more straightforward and cost effective. In some cases, acoustic FWI using reflection data will work sufficient, but it is important to remember that the acoustic reflection coefficient in most cases will behave quite different from the elastic reflection coefficient.

The fourth and most likely reason is related to the initial velocity model and how the FWI algorithm works. The FWI algorithm used in this project was based on a dynamic weighting in the velocity sensitivity kernel and so the gradient will always be dominated by the low-frequency part which usually is represented by refractions and diving waves. Even though the reflections were included in the inversion, the gradient will be dominated by the refractions. Also, as the low-velocity gas plume was not included in the initial velocity model, it seems like the FWI was unable to update this part since the initial velocity model is too far from the reality.

6.2 One-way wave equation migration

As mentioned, WEM expresses the wavefield at a particular depth in terms of the same wavefield existing at a shallower or greater depth, to the recorded wavefield and the wavefield coming

from the source location. Since the wavefield at any depth level only depends on the wavefield at shallower depths, it is impossible for the waves to turn upward because the wavefield would require knowledge of its state at greater depth levels. This will exclude many arrival paths such as multiples, diving waves and refractions as these waves undergo double bounces or continuous refraction (Jones, 2010). All one-way wave equation migrations share this problem; they do not perform a sufficient job of representing wavefields that contain a wide range of angular information, such as steep-dipping reflectors unless they are adjusted (Holberg, 1988). Such adjustments have improved over the last years, using approaches such as tilted plane-wave migration methods (Higginbotham et al., 1985) or modified poststack phase-shift migration methods (Claerbout et al., 1985). Also, one-way wave equations methods do not preserve the amplitudes, meaning that reflectivity information is not preserved in the image. A two-way wave propagator such as reverse time migration is required to solve these problems. A two-way wave equation will better handle all types of waves since the algorithm deals with both up- and downgoing waves that can change direction either on the way down or the way up.

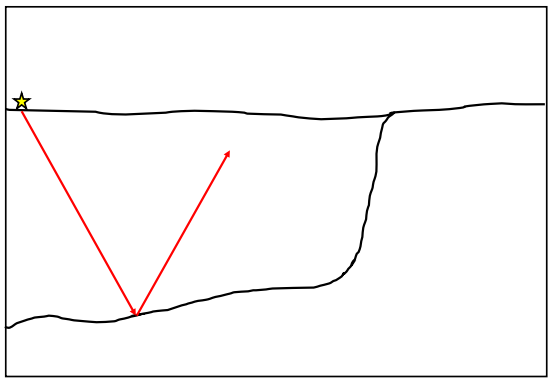

(a) Conventional one-way migration methods assume no change in propagation direction on the way from the surface down to the reflector or on the way back to the surface.

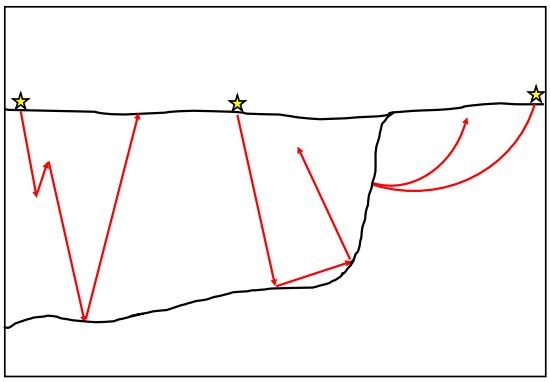

(b) The direction of propagation in two-way migration methods can either bounce on the way down from the surface to the reflector or on the way back to the surface.

Figure 6.1: Simplified one-way and two-way migration methods.

Two-way wave equation migrations have previously shown increased image quality especially in complex geological areas. The algorithm is more complex to write, in addition the computer costs increase notably. In this project, the geology is simple and flat and it is hard to tell if a two-way wave equation migration would have increased the image quality and if the increased

computer cost would have been worth it.

As just described, since one-way methods can not handle refractions, diving waves and multiples must be removed before WEM is performed. The demultiple data used in this project is not the final demultiple data, so there is reason to believe that the data still contains multiples. This must be taken into account when interpreting the WEM results. The algorithm will treat the remaining multiples as primaries and unwanted noise or false structures may be introduced to the image.

6.3 Time-lapse results

The same is true for the time-lapse study. As the WEM data contains remaining multiples, this will introduce false time-lapse results or 4D leakage. Also, since the WEM usually gets affected by acquisition footprints, noise in the migrated seismic may be magnified as a time-lapse response. Ideally, least-squares inversion should have been used on the migrated data before performing time-lapse. The least-squares inversion could have attenuated uneven illumination artifacts related to acquisition and so the time-lapse response would not have been so affected by excessive 4D leakage.

6.4 Further work

In order to understand the migration pattern of the injected CO_2, it is important that the velocity model is reliable and represents the subsurface reflectivity. As mentioned above, uncertainties in our final velocity model should be further investigated. Then, a repeated wave-equation migration should be performed using the final demultiple data as input, instead of a dataset containing multiples. We should in the future, prior to time-lapse, attempt to minimize the acquisition footprints by employing proper seismic processing techniques, such as least-squares inversion. This is most likely to be done by PGS in near future. Also, in order to get more reliable time-lapse results, a more accurate 4D matching should be considered. At this stage, it would be possible to compare previous time-lapse work done by PGS which have been carried out using

PSTM data. Finally, further work remains to be done when interpreting the gas in the migrated images and time-lapse results.

Chapter 7

Conclusions

Storing CO_2 in subsurface reservoirs has previously been considered as very successful, but challenges remain regarding the understanding of the injected CO_2 in the Sleipner field. The physical processes and trapping mechanisms during and after CO_2 injection vary significantly over time, and it is therefore important to monitor the gas to track the gas migration pattern, to prevent unwanted leakage or other damages. High resolution velocity models which can give accurate positioning of reflectors to further improving the interpretation of the gas, is therefore essential.

In this study, a detailed background model was constructed by performing FWI on the monitor data with a frequency band of 2-9Hz. The full waveform inversion was not capable of updating for the low velocities caused by the injected CO_2. Reflected energy was difficult to include in the inversion, as the refracted energy dominated the FWI algorithm.

We believe the initial starting model used for FWI was too far from the true subsurface reflectively. The low-velocity gas bearing layers were not included in the initial velocity model, and so we observed the inversion struggle to update in this area. More time should have been spent on the initial starting model, but time limitations made this difficult.

Based on amplitude differences, colored inversion was performed to introduce the low gas velocities in the model. The final model which accounted for the gas was used as input in forward modelling, but the match between real and modeled data was affected by cycle skipping and so

no further inversion started.

Nevertheless, the colored inversion model was used for migration. The monitor data was migrated with both the background model and the colored inversion model, while the base survey was only migrated with the background model. Comparing the migration results for the monitor data showed that the final model gave flatter gathers, thinner layers as well as higher resolution in the gas saturated layers compared to migration with the background model. The large push-down was also more reduced with the final model compared to the background model. This indicated that the final model better represented the subsurface velocity. Migrating the base survey with the background model showed the subsurface geology before the gas was injected. The gathers were flat indicating that the model did represent the subsurface at this time.

Even though the migration gave good results, different sources of error in the input data was carefully taken into account. Severe footprints in the migrated data oriented in the west-east direction as alternating weak and strong amplitude stripes were related to acquisition geometry and not to geology. This was important to keep in mind when interpreting the WEM results. The acquisition footprints were especially visible in the shallow, but as figure 7.1 shows, the sail line imprint was still visible at the target depth. Also, as the input data for migration contained multiples, this may have caused false structures in the migrated image which may be misinterpreted as true geology. For example, from the monitor data, we noticed several horizons below the gas plume which were affected by remaining multiples.

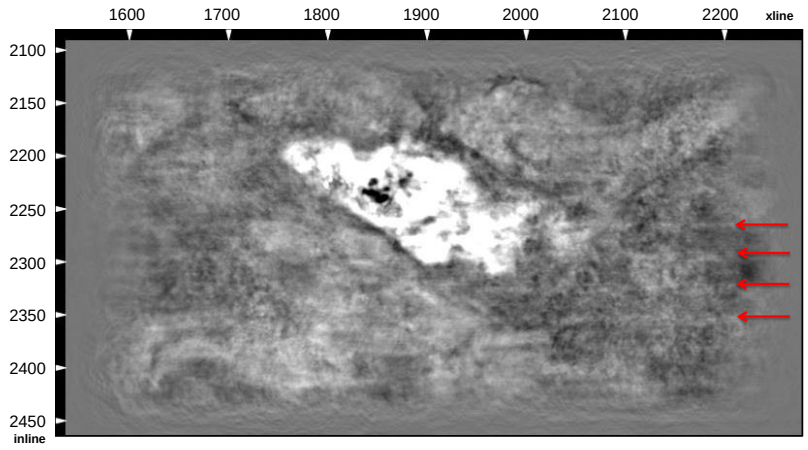

Figure 7.1: Depth slices at 900m over the Sleipner field with one-way wave equation migration. Sail line acquisition footprint seen as lateral stripes indicated by red arrows in the figure.

For the time-lapse study, the CO_2 response itself was very clear, indicating strong confidence in the time-lapse observations. No indication of high amplitude changes in the overburden above the gas was observed, and consequently no leakage of CO_2 had occurred. The seismic after WEM was used for the time-lapse results. Due to remaining multiples and different acquisition geometry in the datasets, unwanted noise and artifacts were magnified in the time-lapse response. Ideally, least-squares inversion should have been used on the migrated data before performing time-lapse to get rid of the excessive 4D leakage and acquisition footprints just described.

References

Arntsen, B. Acoustic full newton waveform inversion.

Arntsen, B. (2015). *Geophysical Analysis TPG4165 Lecture Notes*.

Baklid, A., Korbol, R., Owren, G., et al. (1996). Sleipner vest co2 disposal, co2 injection into a shallow underground aquifer. In *SPE Annual Technical Conference and Exhibition*. Society of Petroleum Engineers.

Claerbout, J. F. (1971). Toward a unified theory of reflector mapping. *Geophysics*, 36(3):467–481.

Claerbout, J. F., Green, C., and Green, I. (1985). *Imaging the earth's interior*, volume 6. Blackwell scientific publications Oxford.

Fichtner, A. (2010). *Full seismic waveform modelling and inversion*. Springer Science & Business Media.

Furre, A.-K. and Eiken, O. (2014). Dual sensor streamer technology used in sleipner co2 injection monitoring. *Geophysical Prospecting*, 62(5):1075–1088.

Gazdag, J. (1978). Wave equation migration with the phase-shift method. *Geophysics*, 43(7):1342–1351.

Ha, W. and Shin, C. (2013). Efficient laplace-domain full waveform inversion using a cyclic shot subsampling method. *Geophysics*, 78(2):R37–R46.

Higginbotham, J. H., Shin, Y., and Sukup, D. (1985). Directional depth migration. *Geophysics*, 50(11):1784–1789.

Holberg, O. (1988). Towards optimum one-way wave propagation1. *Geophysical Prospecting*, 36(2):99–114.

Jones, I. F. (2010). *An introduction to: Velocity model building*. Eage Publications.

Lu, S., Li, X., Valenciano, A., Chemingui, N., and Cheng, C. (2017). Least-squares wave-equation migration for broadband imaging.

Raknes, E. B. (2015a). *Three Dimensional Elastic Full Waveform Inversion*. PhD thesis, NTNU.

Raknes, E. B. (2015b). Three dimensional elastic full waveform inversion.

Ramos-Martinez, J., Chemingui, N., Crawley, S., Zou, Z., Valenciano, A., and Klochikhina, E. (2016). A robust fwi gradient for high-resolution velocity model building. In *SEG Technical Program Expanded Abstracts 2016*, pages 1258–1262. Society of Exploration Geophysicists.

Vedanti, N., Pathak, A., Srivastava, R., and Dimri, V. (2009). Time lapse (4d) seismic: Some case studies. *Earth Science India*, 2:230–248.

Virieux, J. and Operto, S. (2009). An overview of full-waveform inversion in exploration geophysics. *Geophysics*, 74(6):WCC1–WCC26.

Appendix A

Appendix

A.1 Abbreviations

- 4D – Four dimensions. The fourth dimension is time. Also called time-lapse
- FWI – Full waveform inversion
- WEM – One-way wave equation migration
- LSM – Least-squares migration
- PSTM – Pre-stack time migration

- ms – Millisecond
- m – Meter
- s – Seconds
- dB – Decibel
- Hz – Hertz

A.2 The Born approximation

In the framework of the Born approximation, we assume that the subsurface reflectivity, $\mathbf{m}$, can be described as the sum of the starting reflectivity plus a perturbation: $\mathbf{m} = \mathbf{m_0} + \delta\mathbf{m}$. Changing the velocity, will also update the pressure wavefield: $P = P_0 + \delta P$.

Inserting the perturbation model; $\mathbf{m} = \mathbf{m_0} + \delta\mathbf{m}$ and the updated pressure wavefield; $P = P_0 + \delta P$ into the wave equation gives (Arntsen)

$$\nabla^2(P + \delta P) - \frac{1}{(c_o + \delta c)^2}[\ddot{P} + \delta\ddot{P}] = s(\mathbf{x}, t) \tag{A.1}$$

$$\nabla^2(P + \delta P) - \frac{1}{c_0^2\left(1 + \frac{\delta c}{c_0}\right)^2}[\ddot{P} + \delta\ddot{P}] = s(\mathbf{x}, t) \tag{A.2}$$

Assuming δc is much smaller than c

$$\nabla^2(P + \delta P) - \frac{1}{c_0^2}\left(1 - \frac{2\delta c}{c_0}\right)[\ddot{P} + \delta\ddot{P}] = s(\mathbf{x}, t) \tag{A.3}$$

Multiplying out the brackets gives

$$\nabla^2 P + \nabla^2\delta P - \frac{1}{c_0^2}\ddot{P} + \frac{2\delta c}{c_0^3}\ddot{P} - \frac{1}{c_0^2}\delta\ddot{P} + \frac{2\delta c}{c_0^3}\delta\ddot{P} = s(\mathbf{x}, t) \tag{A.4}$$

The first and third term together with the source term is equal to the original wave equation and gets pulled out. We are left with

$$\nabla^2\delta P + \frac{2\delta c}{c_0^3}\ddot{P} - \frac{1}{c_0^2}\delta\ddot{P} + \frac{2\delta c}{c_0^3}\delta\ddot{P} = 0 \tag{A.5}$$

By assume the product of change in wavefield and velocity is small, we neglect $\frac{2\delta c}{c_0^3}\delta\ddot{P}$:

$$\nabla^2\delta P - \frac{1}{c_0^2}\delta\ddot{P} = \frac{2\delta c}{c_0^3}\ddot{P} \tag{A.6}$$

Equation A.6 describes the solution to the forward modeling, $\mathbf{Am} = \mathbf{d}$, in least-squares migration. $\mathbf{m}$ is represented by the unknown velocity δc.

After some calculation, the solution can be written as an integral in terms of Green's function

$$P(\mathbf{x}_r, t) = \int g(\mathbf{x}_r, t; \mathbf{x}, t') \frac{2\delta c(\mathbf{x})}{c_0^3(\mathbf{x})} \ddot{P}(\mathbf{x}, t) d\mathbf{x}. \tag{A.7}$$

A.3 Least-squares migration

Least-squares migration (LSM) uses inverse operators and produces images with fewer artifacts, higher resolution and more accurate amplitudes compared to standard seismic migration. LSM has the advantage of efficient propagation of high frequency seismic data using high-resolution models, for example from full waveform inversion.

The inverse problem $\mathbf{m} = \mathbf{A}^{-1}\mathbf{d}$ is ill-posted and explicit expression for the inverse operator is not available. The adjoint of the modeling operator is often used as an approximation to the inverse. The adjoint process can be expressed as

$$\mathbf{m} = \mathbf{A}^{\dagger}\mathbf{d} \tag{A.8}$$

where † denotes the adjoint operator (conjugate transpose). Least squares-migration on the other hand, implements the full inversion to achieve a more accurate result with a unique generalized inverse of $\mathbf{A}$ found by a least-squares solution.

In order to find the subsurface reflectivity that best describes the data, an approximate solution to an inconsistent system of equations ($\mathbf{Am} = \mathbf{d}$), a well defined notion of nearness is needed. When a solution is demanded and non existing, the best one can do is to find an $\mathbf{m}$ that makes $\mathbf{Am}$ as close as possible to $\mathbf{d}$.

A general definition to least-squares problems can be written as:

If $\mathbf{A}$ is $m \times n$ and $\mathbf{d}$ is in $\mathbb{R}^m$, a least-squares solution of $\mathbf{Am} = \mathbf{d}$ is an $\hat{\mathbf{m}}$ in $\mathbb{R}^n$ such that

$$||\mathbf{d} - \mathbf{A}\hat{\mathbf{m}}|| \leq ||\mathbf{d} - \mathbf{Am}|| \tag{A.9}$$

for all $\mathbf{m}$ in $\mathbb{R}^n$.

The least-squares migration is defined by minimizing the difference between the observed and the modeled data (Lu et al. (2017)).

$$\mathbf{m} = \mathbf{argmin}_{\mathbf{m}} \frac{1}{2} ||\mathbf{d} - \mathbf{Am}||^2{}_{min} \tag{A.10}$$

The LSM iterative updates the reflectivity by migration of the misfit between observed and modeled data. The inversion converges when the modeled data matches the observed data.

By multiplying each side of the original equation 4.2 by the conjugate transpose of $\mathbf{A}$; $\mathbf{A}^\dagger$ to make a square symmetric covariance matrix of $\mathbf{A}$, which is invertible (in a generalized sense), and then solve for m (Jones (2010)):

$$\mathbf{A}^\dagger \mathbf{d} = (\mathbf{A}^\dagger \mathbf{A})\mathbf{m} \tag{A.11}$$

and solving for m:

$$\mathbf{m} = (\mathbf{A}^\dagger \mathbf{A})^{-1} \mathbf{A}^\dagger \mathbf{d} \approx \mathbf{H}^{-1} \mathbf{m}_{\mathbf{mig}} \tag{A.12}$$

Where $\mathbf{H}$ is the Hessian matrix. The currently available solution of the above inverse problem in PGS is by direct inversion of the Hessian matrix by use of point spread functions. The term $\mathbf{H}^{-1}\mathbf{m}_{\mathbf{mig}}$ in equation A.12 is acting as a correction operator which is applied to the migrated image.

Appendix B

Other figures

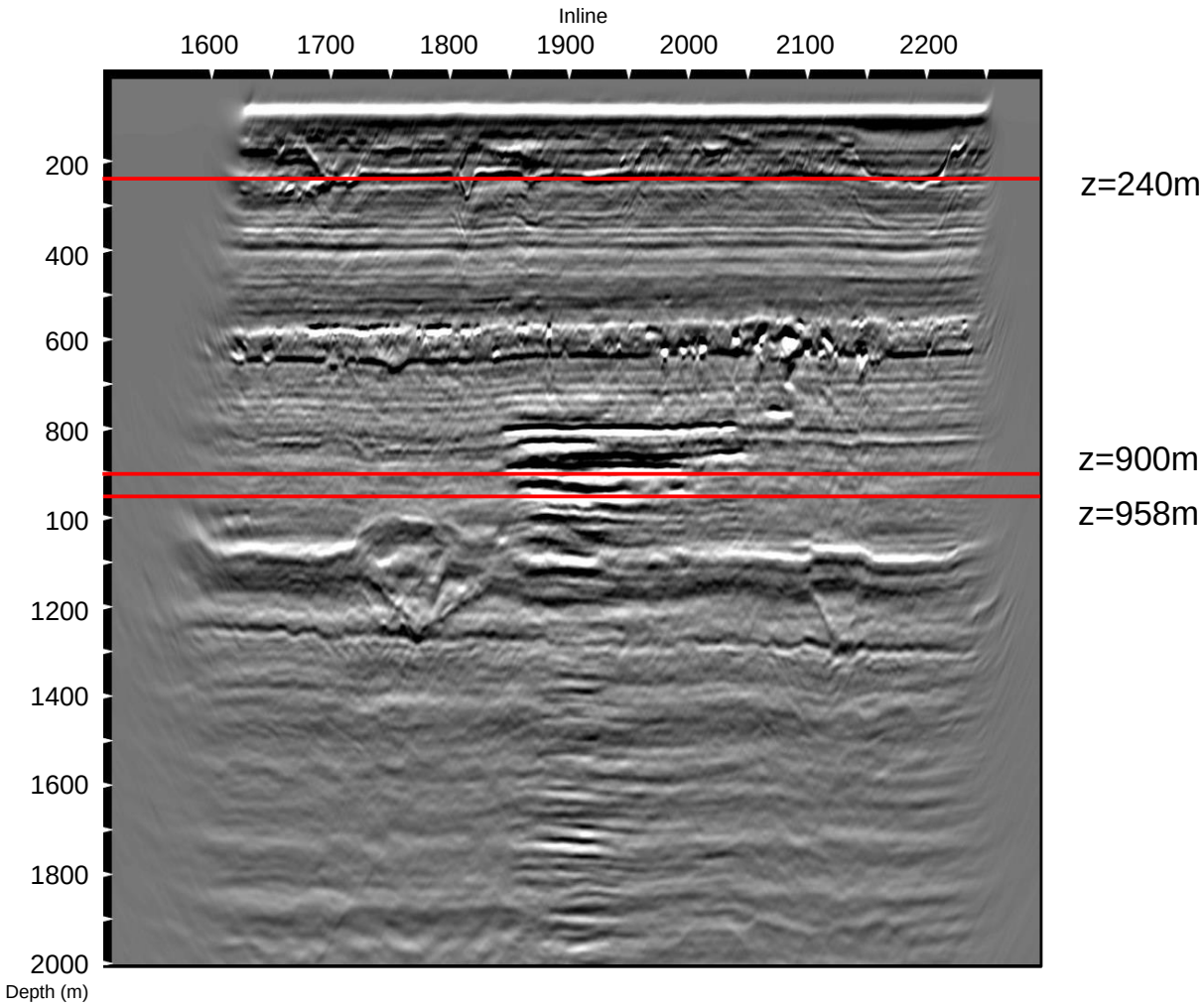

Figure B.1: Inline 2264

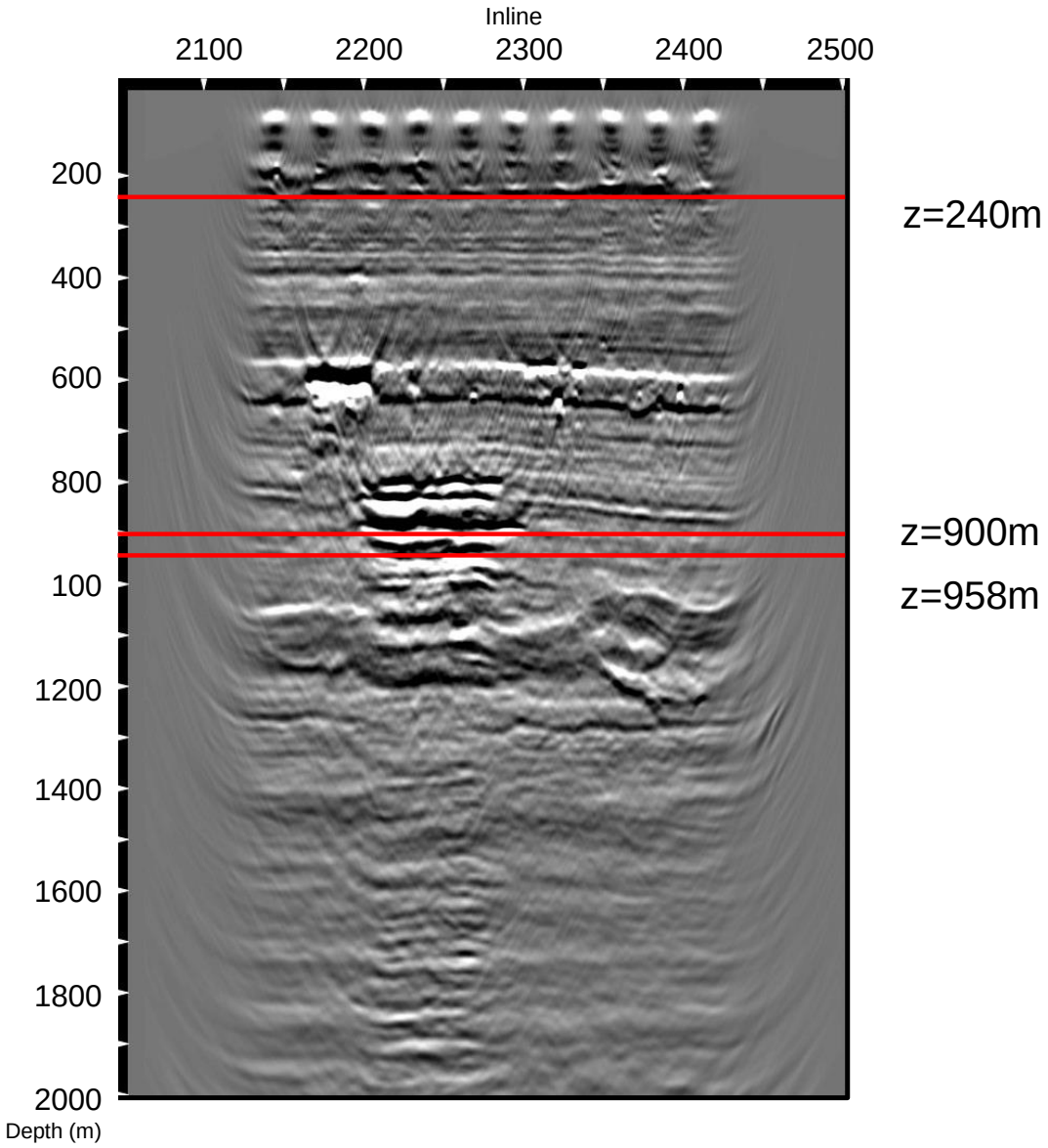

Figure B.2: Xline 1900

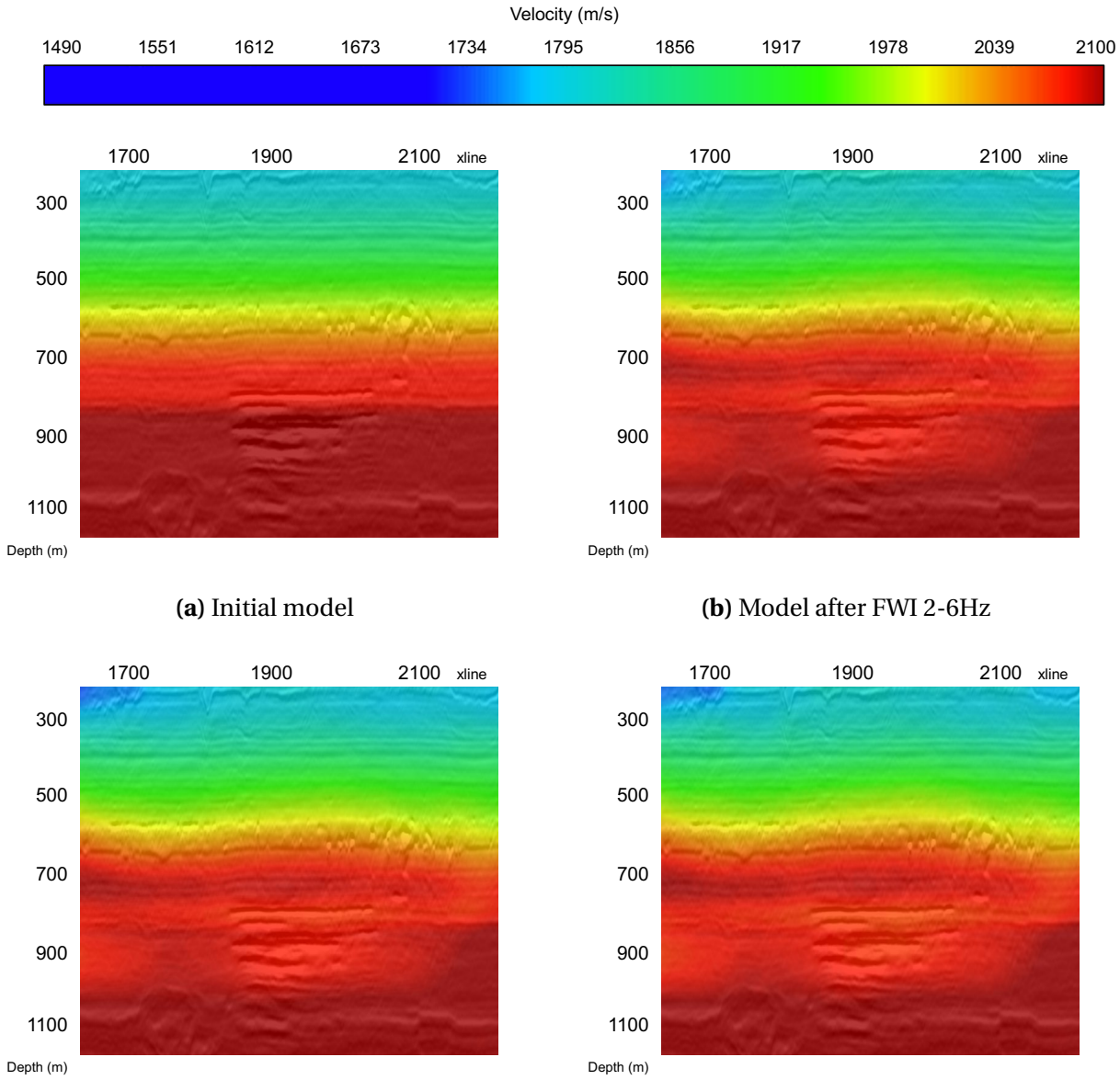

(a) Initial model

(b) Model after FWI 2-6Hz

(c) Model after 2-9Hz

(d) Model after 2-12Hz

Figure B.3: Vertical slices for the different models at inline 2264 with seismic overlayed.

List of Figures